Cell Reports
Medicine

Article

Age-specific induction of mutant p53 drives clonal hematopoiesis and acute myeloid leukemia in adult mice

Graphical abstract

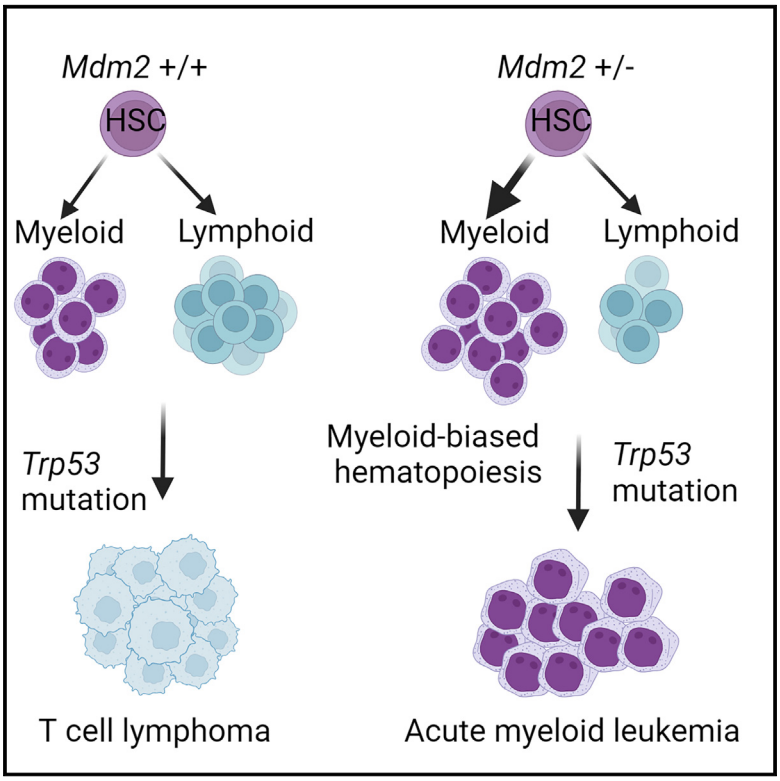

Highlights

- Allele-specific loss of *MDM2* in *TP53*-mutant acute myeloid leukemia (AML)
- *Mdm2* haploinsufficiency collaborates with mutant *Trp53* in AML
- p53-independent mechanism of Mdm2 in controlling the mevalonate pathway
- Targeting the mevalonate pathway enhances the efficacy of MDM2 inhibitors in AML

Authors

Rasoul Pourebrahim, Rafael Heinz Montoya, Hiroki Akiyama, ..., Mihai Gagea, Peter Van Loo, Michael Andreeff

Correspondence

mandreef@mdanderson.org

In brief

Pourebrahim et al. develop two mouse models for p53-mutant acute myeloid leukemia, revealing how Mdm2 interaction and the timing of mutations in blood stem cells influence disease onset and type. This work offers new insights into AML pathogenesis and potential treatment strategies.

Pourebrahim et al., 2024, Cell Reports Medicine *5*, 101558
May 21, 2024
https://doi.org/10.1016/j.xcrm.2024.101558

CellPress

Cell Reports Medicine

CellPress
OPEN ACCESS

Article

Age-specific induction of mutant p53 drives clonal hematopoiesis and acute myeloid leukemia in adult mice

Rasoul Pourebrahim,[1] Rafael Heinz Montoya,[1] Hiroki Akiyama,[1] Lauren Ostermann,[1] Shayuan Khazaei,[1] Muharrem Muftuoglu,[1] Natalia Baran,[1] Ran Zhao,[1] Tom Lesluyes,[2] Bin Liu,[3] Joseph D. Khoury,[4] Mihai Gagea,[5] Peter Van Loo,[2,6,7] and Michael Andreeff[1,8,*]

[1]Section of Molecular Hematology and Therapy, Department of Leukemia, The University of Texas MD Anderson Cancer Center, Houston, TX, USA
[2]Cancer Genomics Laboratory, The Francis Crick Institute, London, UK
[3]Department of Epigenetics and Molecular Carcinogenesis, The University of Texas MD Anderson Cancer Center, Houston, TX, USA
[4]Department of Pathology, Microbiology, and Immunology, University of Nebraska Medical Center, Omaha, NE, USA
[5]Department of Veterinary Medicine and Surgery, The University of Texas MD Anderson Cancer Center, Houston, TX, USA
[6]Department of Genetics, The University of Texas MD Anderson Cancer Center, Houston, TX, USA
[7]Department of Genomic Medicine, The University of Texas MD Anderson Cancer Center, Houston, TX, USA
[8]Lead contact
*Correspondence: mandreef@mdanderson.org
https://doi.org/10.1016/j.xcrm.2024.101558

SUMMARY

The investigation of the mechanisms behind p53 mutations in acute myeloid leukemia (AML) has been limited by the lack of suitable mouse models, which historically have resulted in lymphoma rather than leukemia. This study introduces two new AML mouse models. One model induces mutant p53 and *Mdm2* haploinsufficiency in early development, showing the role of Mdm2 in myeloid-biased hematopoiesis and AML predisposition, independent of p53. The second model mimics clonal hematopoiesis by inducing mutant p53 in adult hematopoietic stem cells, demonstrating that the timing of p53 mutation determines AML vs. lymphoma development. In this context, age-related changes in hematopoietic stem cells (HSCs) collaborate with mutant p53 to predispose toward myeloid transformation rather than lymphoma development. Our study unveils new insights into the cooperative impact of HSC age, *Trp53* mutations, and *Mdm2* haploinsufficiency on clonal hematopoiesis and the development of myeloid malignancies.

INTRODUCTION

TP53 abnormalities are observed in 5%–10% of *de novo* myelodysplastic syndrome (MDS) and AML patients, but the frequency increases up to 40% in older patients or those with therapy-related myeloid malignancies.[1] The mechanisms by which *TP53* mutations lead to the development of AML are not well understood. Previous data from studies with *Trp53* and *Mdm2* knockout mice suggested that once p53 is inactivated, Mdm2 becomes redundant in cells.[2,3] However, recent findings have challenged this established belief, revealing that Mdm2 plays a crucial role in the survival and proliferation of p53-mutated and deleted human cancer cells, such as triple-negative breast cancer.[4]

The regulation of p53 protein by Mdm2 plays a crucial role in maintaining cellular integrity following DNA damage.[5,6] Mdm2 is an E3 ubiquitin ligase that targets p53 for degradation in the 26S proteasome, providing a mechanism for fine-tuning p53 levels after DNA damage.[7–9] Li-Fraumeni syndrome (LFS), caused by germline mutations in the *TP53* gene, is associated with increased susceptibility to developing lymphoid malignancies at a young age, and myeloid malignancies in the setting of therapy-related disease and old age.[10] Similarly, mice with germline *Trp53* mutations also predominantly develop lymphomas rather than leukemias,[11] further emphasizing the role of germinal p53 mutations in lymphoma predisposition. Yet, the role of p53 and Mdm2 in hematopoietic differentiation and their link to the development of specific hematological malignancies have yet to be fully elucidated.

In this study, we explored the impact of *Mdm2* haploinsufficiency on the development of lymphoma vs. AML in the presence of *Trp53* R172H mutation. Our analysis revealed concurrent heterozygous loss of *MDM2* in *TP53*-mutated AML, along with a significant enrichment of $Mdm2^{SNP309}$ in *TP53*-mutant AML. We show that *Mdm2* haploinsufficiency leads to myeloid-biased hematopoiesis, which cooperates with somatic *Trp53*-mutations in the development of AML. Furthermore, we uncovered a novel function of Mdm2 in regulation of the mevalonate pathway and demonstrate that its inhibition promotes myeloid differentiation, independently of its role in p53 regulation. Through a series of complementary genetic models, we show that the age of mice is a critical factor in determining the transformation to myeloid

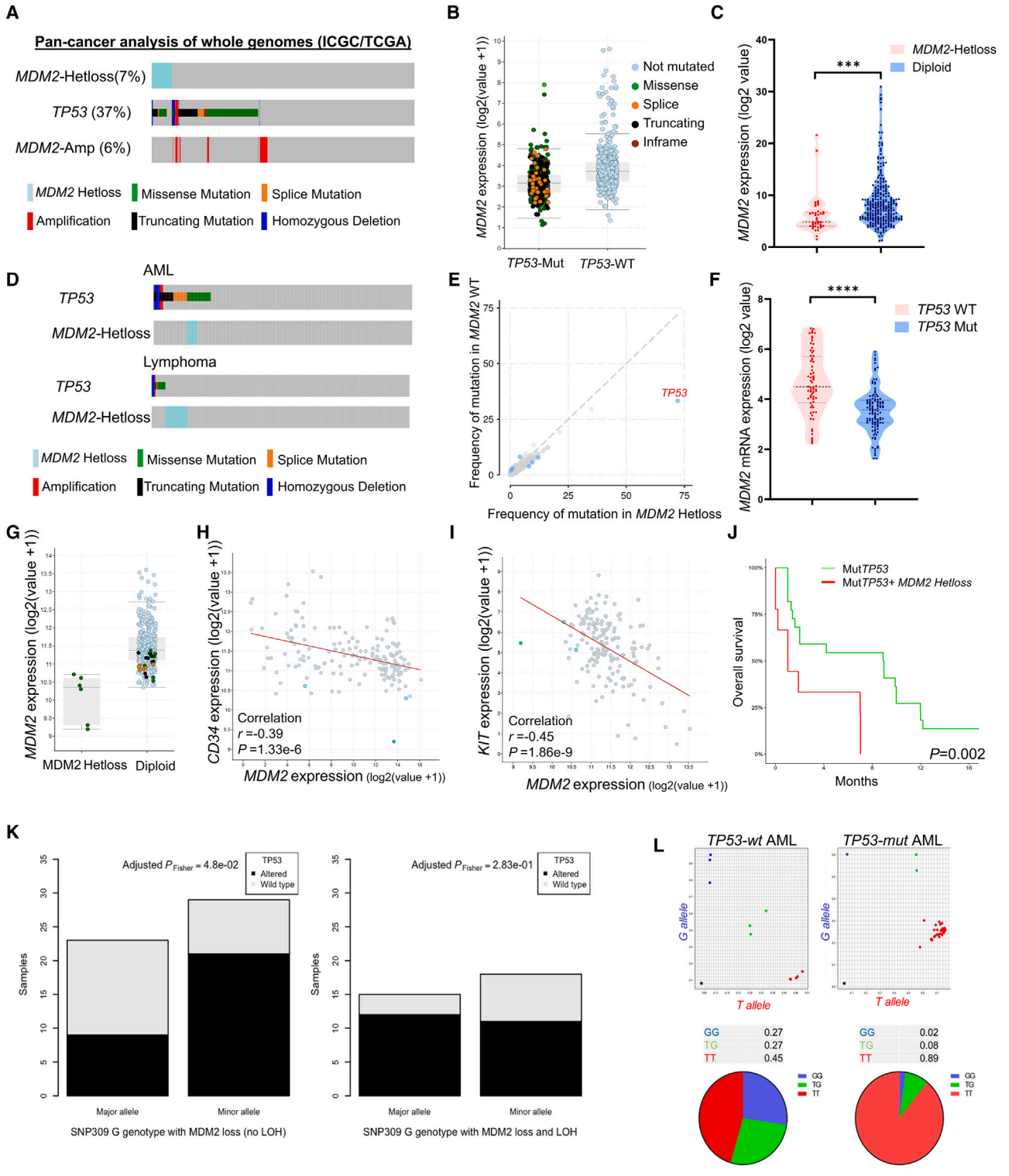

Figure 1. Analysis of *TP53* mutations, *MDM2* alterations, and *MDM2* expression patterns in cancer

(A) Frequency of *TP53* mutations and *MDM2* copy number alterations across various cancer types using whole-genome analysis of ICGC/TCGA Pan-Cancer data.

(B) Expression of *MDM2* in *TP53*–wild-type (WT) and *TP53*-mutant (Mut) cases in pan-cancer analysis of whole genomes.

(C) Relative expression of *MDM2* mRNA based on *MDM2* allele status pan-cancer analysis of whole genomes, ***$p < 0.001$.

(legend continued on next page)

vs. lymphoid malignancies in the context of p53 mutations. Together, our findings present a valuable mouse model for dissecting the role of mutant p53 in AML and offer important insights into the impact of *Mdm2* haploinsufficiency on myeloid-biased hematopoiesis, potentially guiding the development of therapeutic strategies for *TP53*-mutant AML.

RESULTS

Frequency and association of *MDM2* alterations and *TP53* mutations and allele-specific characteristics of *MDM2*^{SNP309} in AML

To assess the significance of *MDM2* alterations and the potential implications of *MDM2* haploinsufficiency in AML, we conducted an analysis using data from the Pan-Cancer Analysis of Whole Genomics study.[12] Our objective was to determine the frequency of *MDM2*-Hetloss specifically in *TP53* mutant tumors. Among the 2,583 patients examined, we observed *MDM2*-Hetloss in approximately 7% of all cancers. However, *TP53*-mutant cases exhibited *MDM2* Hetloss in more than 17% of instances, indicating a strong association (log2 odds ratio = 2.04, $p < 0.001$) (Figure 1A). It is worth noting that no homozygous deletions of *MDM2* were detected in any cancer types, suggesting the essential nature of *MDM2*, even in *TP53*-mutant tumors, which has been previously reported.[13] We also assessed the transcript levels of *MDM2* with respect to *TP53* mutation status and found that *MDM2* expression levels are significantly lower in *TP53*-mutant tumors (t test, $p = 0.0001$) (Figure 1B). In the *TP53*-mutant group, *MDM2* expression was significantly lower in *MDM2*-Hetloss cases compared with *MDM2*-diploid cases (t test, $p = 0.001$) (Figure 1C). Additionally, we searched for available AML datasets on cBioPortal (400 cases) and found that MDM2-Hetloss was concomitant with TP53 missense mutations (log2 odds ratio >3, $p < 0.001$) (Figure 1D). This association was not present in lymphomas, where we found MDM2-Hetloss and TP53 mutations to be mutually exclusive, suggesting that the observed *MDM2* copy number changes may have a specific link to the myeloid lineage (Figure 1D). Among AML patients with *MDM2*-Hetloss, *TP53* mutations were the most frequently observed mutation (Figure 1E). To validate these genomic findings, we expanded our analysis to a *TP53*-mutant AML dataset consisting of 187 AML cell lines documented in the Cancer Cell Line Encyclopedia.[14] The AML cell lines with *TP53* mutations exhibited significantly lower *MDM2* expression compared with *TP53* wild-type cell lines ($p = 0.0001$) (Figure 1F).

To investigate if the reduced expression of *MDM2* in *TP53*-mutant patients is due to *MDM2*-Hetloss or impaired transcriptional activity of TP53 resulting from mutations, we compared *MDM2* expression in subjects with *MDM2*-Hetloss with those with a diploid *MDM2* status. Significantly lower *MDM2* expression was observed in *TP53*-mutant/*MDM2*-Hetloss cases compared with *TP53*-mutant/*MDM2*-diploid cases ($p = 0.001$) (Figure 1G). This indicates that in *TP53*-mutant patients, *MDM2* levels are predominantly influenced by *MDM2* copy number. Further analysis was conducted to determine whether *MDM2*-Hetloss is linked to a specific phenotype in *TP53*-mutant AML. As depicted in Figures 1H and 1I, an inverse relationship was found between *MDM2* levels and the expression of CD34 and KIT, suggesting a possible role in the differentiation of leukemia cells. Moreover, a significant correlation was found between *MDM2*-Hetloss and lower survival rates ($p = 0.002$) (Figure 1J), suggesting the potential prognostic significance of *MDM2*-Hetloss in *TP53*-mutant AML.

Next, we aimed to investigate whether *MDM2* loss of heterozygosity (LOH) exhibited allele-specific characteristics or varied between alleles of *MDM2* single nucleotide polymorphisms (SNPs), with particular focus on *MDM2*^{SNP309} (rs2279744; T>G). *MDM2*^{SNP309} is located in the intronic promoter region of *MDM2* (Figure S1A) and has been associated with increased *MDM2* expression and earlier cancer onset in patients with LFS and sporadic cancers.[15] We analyzed the *MDM2*^{SNP309} genotype within the pan-cancer analysis of whole genomes (PCAWG) cohort. Due to the limited availability of *TP53*-mutant AML cases (only eight) in a curated list of 2,658 PCAWG cases, we leveraged whole-genome sequencing data to achieve sufficient statistical power. Our analysis revealed similar patterns across the T/T, T/G, and G/G genotypes, indicating no significant association between the *MDM2*^{SNP309} genotype and *TP53* inactivation, alteration, or wild-type status ($P_{chi2} = 0.71$; Figure S1B). We also examined the relationship between *MDM2* copy number status and *TP53* mutational status within the T/T and G/G genotypes. In a wild-type *TP53* context, we observed a higher frequency of *MDM2* losses in the G/G genotype (13.22%) compared with the T/T genotype (7.66%) (adjusted P_{Fisher} test = 3.99e−2; Figure S1C). Subsequently, we assessed *MDM2* allelic imbalances in T/G germline cases and found that the G allele was retained on the major allele in 64% of wild-type *TP53* cases, whereas only 30% of altered-*TP53* cases exhibited this pattern in losses without LOH (Figure 1K). Of note, no significant differences in T/G were observed in losses with LOH.

Additionally, we investigated the *MDM2*^{SNP309} T/G genotype in bone marrow samples from AML patients, distinguishing between those with wild-type ($n = 10$) and mutant *TP53* ($n = 46$).

(D) Frequency of *TP53* mutations and *MDM2* copy number alterations in patients with AML and lymphoma, sourced from cBioPortal for Cancer Genomics.
(E) Frequency of mutations in different genes categorized by *MDM2* WT and *MDM2* LOH, retrieved from cBioPortal.
(F) Relative expression of *MDM2* based on TP53 status using data from the Cancer Cell Line Encyclopedia, ****$p < 0.0001$.
(G) *MDM2* expression in AML samples, highlighting cases with mutant *TP53*: green for missense, brown for splice, and black for truncation mutations.
(H and I) Scatter diagram graphs the correlation of *CD34* and *KIT* versus *MDM2* at the mRNA levels in patients with AML (TCGA).
(J) Overall survival of p53 mutant AML patients with or without *MDM2* LOH.
(K) Bar plot displaying the distribution of the G allele on the major or minor allele in germline T/G cases and in the context of somatic *MDM2* loss, depending on *TP53* mutational status (altered or wild type) and the presence or absence of the T allele (no LOH; left) or its absence (LOH; right). This demonstrates a significant enrichment for the G allele on the minor allele in altered *TP53* cases without LOH (adjusted $P_{Fisher} = 4.8e-2$).
(L) Allele-specific expression analysis of GG (blue), TG (green), and TT (red) in indicated patient samples.

Our findings revealed that the T/T genotype was present in 45% of wild-type *TP53* cases, while 89% of mutant *TP53* cases exhibited the T/T genotype, indicating selective loss of the G allele in *TP53*-mutant AML (Figure 1L). These results suggest an association between allele-specific loss of the G allele and *TP53* mutations in various cancer types and AML patients. Together, these data reveal a strong association between *MDM2*-Hetloss and *TP53* mutations in AML, indicating functional implications. Additionally, allele-specific loss of the G allele suggests a link between *MDM2* expression levels and *TP53* mutations across various cancer types and AML.

Mdm2 haploinsufficiency cooperates with mutant p53 to promote the development of AML

Building on the observed correlation between *MDM2* expression levels and *TP53* mutations in AML, we developed specific genetic models to further elucidate the potential interplay between *Mdm2* levels and *Trp53* mutations, thereby enhancing our understanding of AML pathogenesis. As a brief introduction, the gain-of-function (GOF) activity of mutant p53 has been largely studied through comparison of mice harboring a conditional mutant *Trp53* allele known as *LSL-Trp53*^{R172H}.[16] Hematopoietic-specific induction of *LSL-Trp53*^{R172H} results in thymic lymphoma in most animals.[17] However, the LSL cassette in *LSL-Trp53*^{R172H} mice leads to *Trp53* heterozygosity in the whole mouse, allowing for a heterozygous *Trp53* microenvironment that facilitates tumorigenesis.[18] To tackle this challenge, we utilized an inducible mutant *Trp53*^{R172H} allele, which we refer to as "wmR172H" (where "wm" denotes the transition from wild type to mutant). This allele features an R172H mutation, analogous to the R175H mutation in humans, positioned downstream of a wild-type *Trp53* cDNA sequence, which is in turn flanked by *loxP* sites (Figure 2A). This design ensures the maintenance of wild-type *Trp53* expression until recombination occurs.[19,20] To evaluate the impact of *Trp53* LOH and *Mdm2* haploinsufficiency in our model, we utilized the *Trp53*^{fl} [21] and *Mdm2*^{fl}[22] respectively. To monitor recombined cells in mice, we utilized an *mTmG* allele, a fluorescent reporter with a tdTomato (mT) cassette. Upon *Cre*-mediated recombination, this cassette is replaced by a green fluorescent protein (mG) cassette (Figure 2A).

We initially assessed the impact of *Trp53* mutation/loss in early hematopoietic stem cells (HSCs) using the *Vav-Cre* system. Two mouse cohorts were generated: one with a conditional *Trp53* mutant allele exhibiting*Trp53* LOH *(Vav-Cre;Trp53*$^{wmR172\ H/fl}$), and another with homozygous *Trp53* floxed alleles (*Vav-Cre;Trp53*$^{fl/fl}$), allowing us to compare the effects of p53 mutation vs. complete loss of p53 in HSCs. Some mice also carried the *mTmG* allele for tracking. To validate our model, we analyzed E10.5 *Vav-Cre-mTmG* embryos and confirmed successful recombination of the *mTmG* allele in the aortogonadal mesenchyme and fetal liver by fluorescence microscopy (Figure S2). Mice with *Trp53* mutations and *Trp53* deletion introduced early in life developed lymphoma with complete penetrance, suggesting that the mutation or deletion of *Trp53* at an early age is more likely to result in the development of lymphoma (Figure 2B). Immunohistochemical analysis of lymphoma tissue showed nuclear p53 staining and flow cytometry confirmed CD3 expression and absence of CD11b in lymphoma cells (Figure 2C). The Kaplan-Meier survival analysis revealed comparable survival of *Vav-Cre;Trp53*$^{wmR172\ H/fl}$ mice to that of *Vav-Cre*;*Trp53* $^{fl/fl}$ mice, indicating that there was no GOF of mutant p53 in this model (Figure 2D). Both models had full penetrance of thymic lymphoma, suggesting that the loss of p53 function alone is sufficient to drive lymphoma development in these mice. This observation is consistent with previous reports comparing *Trp53*^{null} with *Trp53*^{R172H} mice in which *Trp53* was deleted or mutated in the whole body.[23–25] The absence of AML in both cohorts indicates that additional genetic aberrations may be necessary in this context for the development of AML.

Next, we aimed to explore the phenotype of *Mdm2* haploinsufficiency and *Trp53* mutations in early HSCs. We crossed mice carrying the *Mdm2*^{fl} alleles,[22] with progeny from *Trp53*$^{wmR172\ H/fl}$ to generate *Vav-Cre;*Mdm2$^{+/fl}$; *Trp53*$^{wmR172\ H/fl}$ mice (referred to as *Vav-Mdm*$^{fl/+}$;*p53*$^{mut/fl}$), some of which also carried the mTmG allele for tracing. *Vav-Mdm*$^{fl/+}$;*p53*$^{mut/fl}$ mice developed AML with full penetrance, characterized by myelomonocytic leukemia cells infiltrating both bone marrow (BM) and liver (Figure 2E; Table S1). Three out of 12 mice succumbed to lymphoma. However, analysis of DNA isolated from tumor tissue revealed a lack of recombination of the *Mdm2* allele in the tumor. Histopathological analysis of BM, spleen, and liver samples revealed myeloid-derived leukemias (Figure 2F). Some mice showed multiclonality with the presence of more than one type of morphologic nonlymphoid hematopoietic neoplasm. Immunostaining analysis showed strong nuclear expression of mutant p53 in the BM (Figure 2G). Flow cytometry analysis revealed a $CD3^{-}$,$CD11b^{+}$, $Ly6G^{+}$ phenotype, consistent with our histopathology findings (Figure 2H). Western blot analysis of a handful of spleen samples revealed high levels of mutant p53 (Figure 2I). Myelomonocytic AML features were observed in BM samples from *Vav-Mdm*$^{fl/+}$;*p53*$^{mut/fl}$ mice, with GFP+ leukemic cells invading periosteum and muscles (Figure S3A). Immunostaining displayed a highly proliferative disease, with p53 accumulation in most malignant BM cells (Figures 2J and 2K). We observed a few clusters of $CD3^{+}$ cells in the BM indicating suppressed lymphoid lineage (Figure S3B). Clonal expansion of p53-mutant AML cells was heterogeneously distributed throughout the BM (Figures S3C and S3D). *Mdm2* haploinsufficiency significantly extended survival of p53-mutant mice compared with *Mdm2*-diploid p53-mutant mice (p = 0.01)(Figure 2L). Notably, mice with the deletion of both *Mdm2* alleles (*Vav-Mdm*$^{fl/fl}$;*p53*$^{mut/fl}$) developed lymphoma, a phenotype comparable to that of *Vav-cre*;*p53*$^{mut/fl}$ mice, suggesting that the complete loss of *Mdm2* does not directly contribute to the development of AML. Together, these findings confirm that *Mdm2* haploinsufficiency and *Trp53* mutations synergistically induce aggressive AML with full penetrance.

Trp53 somatic mutation in adult HSCs leads to pre-leukemic clonal expansion

To explore the clonal evolution of p53 mutant subclones and their progression into myeloid malignancies, we created an inducible mouse model using the *Mx1-cre* driver and polyinosinic:polycytidylic acid (pIpC) induction. The inducible conditional mouse model replicates clonal hematopoiesis by inducing somatic mutations in a fraction of adult HSCs at about 4 months of age, which is equivalent to young adult humans, and track

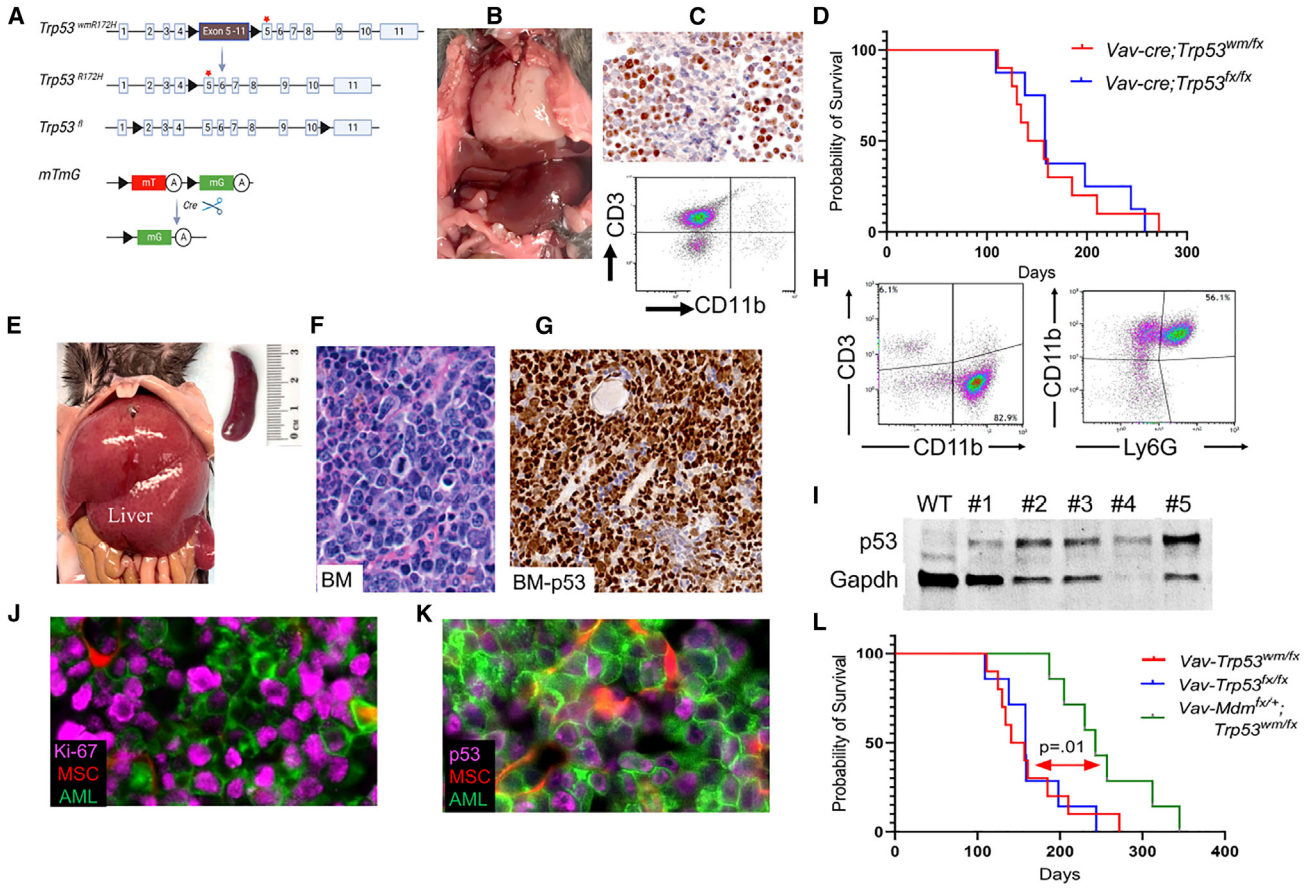

Figure 2. Overview of alleles and pathological findings in a novel p53 mutant AML mouse model

(A) Schematic representation of the genetic modifications in the mouse model. The activation of Cre recombinase under the *Vav1* promoter leads to deletion of wild-type *Trp53* cDNA flanked by *loxP* sites (black triangles) resulting in a *Trp53*-mut allele. The diagram also shows the recombination of the *mTmG* reporter allele, facilitating GFP expression in hematopoietic cells, with "mT" for membranous tomato, "mG" for membranous GFP, and "A" indicating a polyadenylation sequence. The red star marks the *Trp53* R172H mutation on exon 5.

(B) Image of a white thoracic lymphoma mass in a *Vav-Cre;Trp53*$^{fl/wmR172H}$ mouse.

(C) Immunohistochemistry for p53, showing nuclear accumulation in lymphoma cells. Flow cytometry analysis identifying a distinct CD3$^+$ T lymphocyte population, with absence of CD11b$^+$ myeloid cells.

(D) Kaplan-Meier survival curve with a *p* value of 0.2 from the log rank (Mantel-Cox) test, showing the overall survival rate of the mice.

(E) Representative image of AML infiltration in liver and spleen of moribund *Vav-Cre;Mdm2*$^{+/fl}$*;Trp53*$^{fl/wmR172H}$ mice.

(F) Hematoxylin and eosin (H&E)-stained bone marrow (BM) section from the AML mouse depicted in (J), showing characteristic features of AML.

(G) Immunostaining for p53 protein, visualized as brown staining, demonstrates the presence of p53 in leukemia cells within bone marrow (BM).

(H) Flow cytometry analysis of CD3, CD11b, and Ly6G markers in the bone marrow of AML mice.

(I) Western blot analysis of p53 protein expression in BM samples comparing p53 protein levels in p53 wild-type control and five AML samples.

(J) Immunofluorescence analysis of Ki-67 in BM. MSCs, mesenchymal stromal cells.

(K) Mutant p53 accumulation in GFP-positive AML cells in BM sections.

(L) Kaplan-Meier analysis of overall survival of the indicated mice. $p = 0.01$, log rank (Mantel-Cox) test.

the recombined cells using the *mTmG* allele (Figure 3A). Initially, we confirmed that *Mx1-cre* effectively targets HSCs in the BM of *Mx1-cre;mTmG* mice. Analysis of BM cells from these mice revealed that the GFP+ population was present within the CD150$^+$/Lin$^-$/Sca1$^+$/c-Kit$^+$ (LSK) cell population, indicating the successful targeting of the hematopoietic stem cell compartment by the *Mx1-cre* driver (Figure S4A). This finding is consistent with previous reports demonstrating the effectiveness of the *Mx1-cre* system *in vivo*.[26] Fluorescence microscopy analysis of the BM displayed clear evidence of efficient recombination of the *mTmG* allele, as indicated by the presence of clonal clusters of GFP+ cells (Figure 3B). The GFP+ cells were detectable throughout the BM and formed distinct colonies. The presence of GFP+ cells was also detected in the peripheral blood (PB), and spleen (Figure 3C).

Next, we investigated the clonal evolution of p53 mutant clonal hematopoiesis by generating cohorts of *Mx1-Cre;mTmG* and *Mx1-Cre;Trp53*$^{wmR172\ H/fl}$*;mTmG* mice, and analyzing PB samples on a monthly basis, starting at 4 months of age. The population of p53-mutant (GFP+) cells increased over time (Figure 3D). Flow cytometry analysis of PB after 3 months revealed an increased myeloid population defined as CD11b+ (Figure 3E).

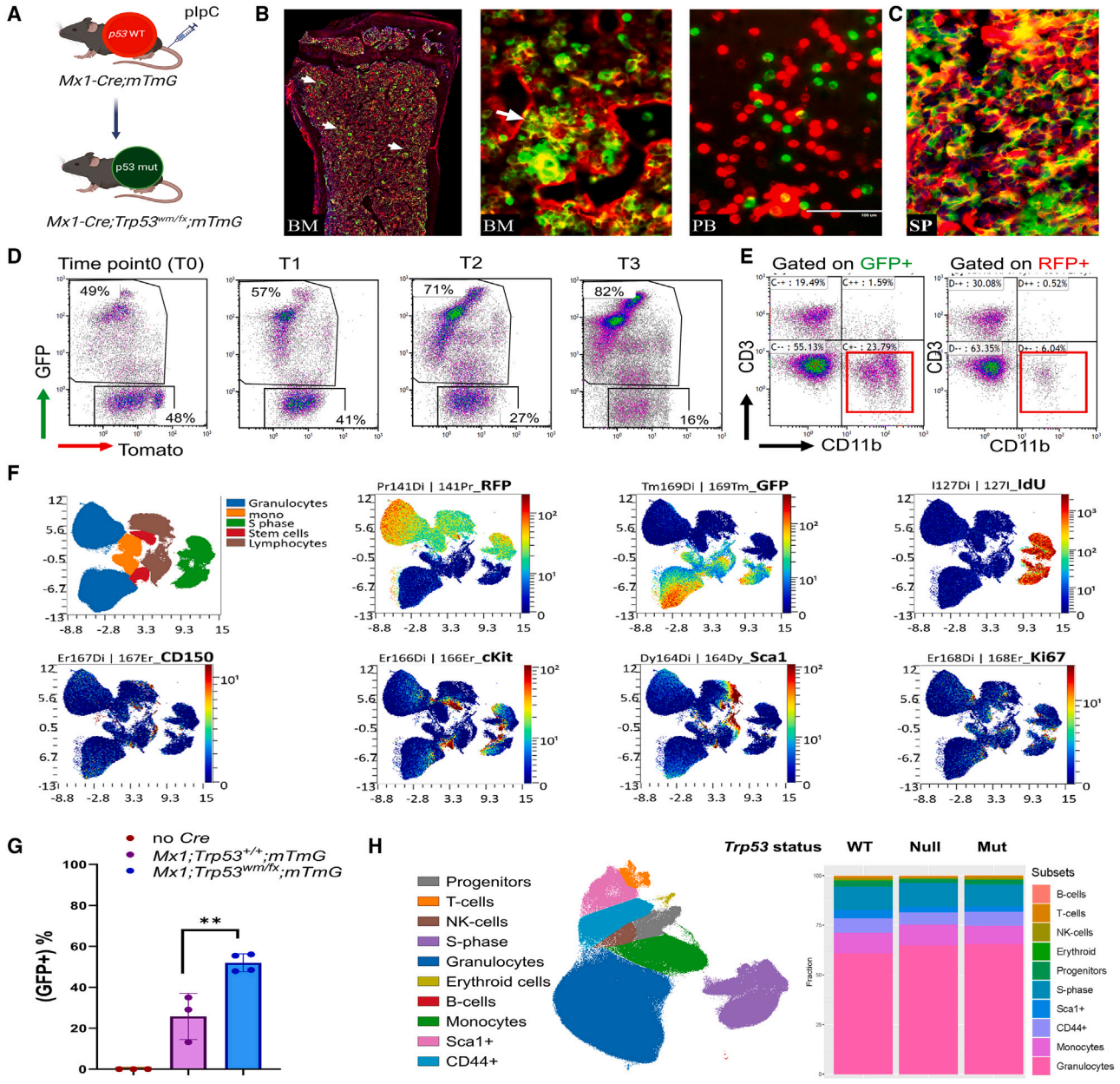

Figure 3. Clonal evolution and generation of a p53 mutant clonal hematopoiesis mouse model

(A) The schematic outlines the creation of the *Trp53*^{R172H} clonal hematopoiesis model in adult HSCs. Following pIpC injection, *Cre* recombinase expressed under the *Mx1-Cre* promoter induces recombination in hematopoietic cells, leading to a fluorescence switch in the *mTmG* allele from red (tdTomato) to green (GFP), simultaneously converting wild-type p53 to its mutant form.

(B and C) (B) Direct fluorescence image of the bone marrow of *Mx1-Cre;Trp53*$^{wmR172\ H/fl}$*;mTmG* mouse showing the distribution of GFP+ cells in the bone marrow (BM), peripheral blood (PB), and (C) spleen (SP). High magnification displaying a colony of GFP+ cells marked by white arrow.

(D) Flow cytometry plots showing the expression of GFP and Tomato in the peripheral blood of *Mx1-Cre;Trp53*$^{wmR172\ H/fl}$*;mTmG* mice at different time points.

(E) Flow cytometry plots of CD3 and CD11b expression gated on GFP or RFP in (D).

(F) tSNE plots representing a CyTOF analysis of the indicated marker distribution in BM.

(G) Graph showing the percentage of GFP+ cells in the peripheral blood of indicated mice over 3 months after pIpC injection. The data are presented as mean ± standard deviation.

(H) UMAP plot showing the cell subsets detected in pooled BM samples isolated from *Mx1-Cre;mTmG* (p53 wild-type), *Mx1-Cre;Trp53* $^{fl/fl}$*;mTmG* (p53 null), and *Mx1-Cre;Trp53*$^{wmR172\ H/fl}$*;mTmG* (p53 mutant) mice subjected to UMAP dimension reduction. Each linage is marked by colors indicating cell type. The stacked bar plots summarize the subset frequencies in indicated genotypes.

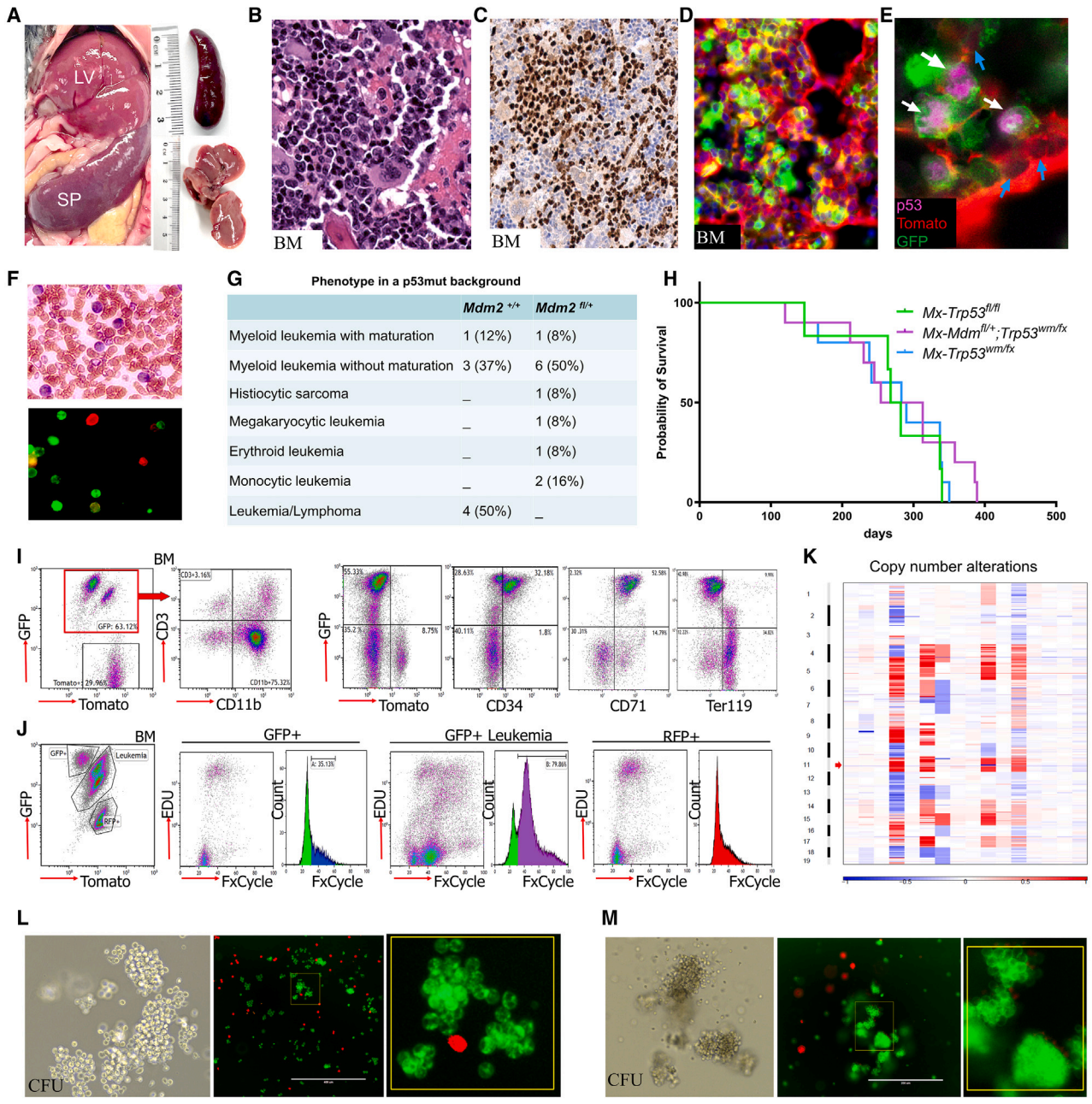

	Mdm2 $^{+/+}$	*Mdm2* $^{fl/+}$
Myeloid leukemia with maturation	1 (12%)	1 (8%)
Myeloid leukemia without maturation	3 (37%)	6 (50%)
Histiocytic sarcoma	_	1 (8%)
Megakaryocytic leukemia	_	1 (8%)
Erythroid leukemia	_	1 (8%)
Monocytic leukemia	_	2 (16%)
Leukemia/Lymphoma	4 (50%)	_

Figure 4. Characterization of AML development in *Mx1-Cre;Trp53*$^{wmR172\ H/fl}$*;mTmG* mice

(A) Infiltration of AML cells into the liver (LV) and spleen (SP), indicative of AML development, is shown.

(B) Hematoxylin and eosin (H&E)-stained sections of bone marrow (BM) showing extensive leukemia cell infiltration.

(C) p53 protein immunostaining in leukemia cells in BM.

(D) Direct fluorescence image of BM depicting colonies of GFP+ cells. The stromal cells and normal hematopoietic cells are labeled with tomato fluorescence.

(E) Fluorescent imaging of p53 immunostaining in BM shows GFP+ hematopoietic cells expressing mutant p53 protein (magenta) among Tomato+ stromal cells.

(F) Peripheral blood smear and fluorescence imaging of GFP+ blast cells.

(G) Table representing the phenotype of different leukemia subtypes in p53 mutant AML mice with indicated Mdm2 genotypes.

(H) Kaplan-Meier analysis of overall survival of the indicated mice.

(I) Flow cytometry analysis of BM for indicated markers showing the expansion of myeloid and erythroid markers within the GFP+ population.

(J) DNA content analysis in selected BM cell populations showing higher DNA content in p53 mutant AML cells (GFP+) compared with normal BM cells (RFP+).

(K) Heat map of copy number variation in bone marrow cells derived from *Mx1-Cre;Trp53*$^{wmR172H/fl}$*;mTmG* mice with AML. Each row represents a separate bone marrow sample, while each column represents specific genomic regions. The color scale indicates the relative copy number, with shades ranging from blue (deletion) to red (amplification).

(legend continued on next page)

To identify specific lineages that were expanded in p53 mutant clonal hematopoiesis, we isolated BM samples from *Mx1-Cre;mTmG* (p53 wild-type), *Mx1-Cre;Trp53*$^{wmR172\ H/fl}$*;mTmG* (p53 mutant) and *Mx1-Cre;Trp53* $^{fl/fl}$*;mTmG* (p53 null) mice and performed CyTOF analysis using a panel of 31 antibodies (Table S2). Antibodies specific to RFP and GFP were employed to distinguish the p53-mutant (GFP+) and p53 wild-type (RFP+) populations (Figure 3F). The p53 wild-type group showed relatively stable population levels over time, whereas the p53 mutant population displayed a significant expansion with increasing duration following polyinosinic:polycytidylic acid (pIpC) injection (Figure 3G). The CyTOF analysis revealed a slight increase in the myeloid lineage in p53 mutant and null mice compared with p53 wild-type (Figures 3H and S4B). We did not observe a significant expansion of a specific stem/progenitor cell population in p53 mutant GFP+ cells. These findings indicate that loss of p53 function may contribute to alterations in hematopoietic lineage development, without causing a dramatic shift in the stem cell population. The overall increase in the myeloid population may indicate a transformation occurring in the myeloid progenitors. Together, these data highlight the significant impact of *Trp53* mutation on the clonal expansion and evolution of HSCs into myeloid lineage within an adult mouse model.

Clonal expansion of p53 mutant cells and development of myeloid malignancies in adult HSCs

We expanded the cohorts of *Mx1-Cre;Trp53*$^{wmR172H/+}$*;mTmG* mice (referred to as *Mx-p53*$^{H/+}$), *Mx1-Cre;Trp53*$^{wmR172\ H/fl}$*;mTmG* mice (referred to as *Mx-p53* $^{mut/fl}$), and *Mx1-Cre;Mdm2*$^{fl/+}$*:Trp53*$^{wmR172\ H/fl}$*;mTmG* mice (referred to as *Mx-Mdm-p53*$^{mut/fl}$) and injected them with pIpC to induce the *Mx1-Cre.* Then, we closely monitored them to observe the development of leukemia in these mice cohorts. After a follow-up period of over a year, the *Mx-p53*$^{mut/fl}$ and *Mx-Mdm-p53*$^{mut/fl}$ mice developed various myeloid malignancies (Figure 4A). In contrast, the *Mx-p53*$^{H/+}$ mice did not develop similar transformations during the observation period. These findings suggest that the loss of the wild-type *Trp53* allele was a crucial factor in the transformation process. *Mx-p53*$^{mut/fl}$ mice displayed a significant expansion of myeloid cells in the BM, categorized as myeloid leukemia with or without maturation, aligning with the Bethesda proposals for classifying nonlymphoid hematopoietic neoplasms in mice[27] (Figures 4B and S5A). Immunostaining of the BM confirmed the accumulation of the mutant p53 in leukemic clones (Figure 4C), which were scattered throughout the bone marrow (Figure S5B), while normal stromal and hematopoietic cells (Tomato-positive) did not show p53 positivity (Figure 4E). GFP+ leukemia blast cells were observed in the PB, indicating the progression and systemic spread of the disease (Figures 4D and 4F). The *Mx-p53*$^{mut/fl}$ mice exhibited a significant incidence of mixed leukemia/lymphoma phenotype (50%). In contrast, all *Mx-Mdm-p53*$^{mut/fl}$ mice presented with myeloid malignancies, showing no expansion of the lymphoid lineage (Figure 4G). The *Mx-Mdm-p53* $^{fl/fl}$ mice (n = 3) developed leukemia with the same penetrance as *Mx-Mdm-p53*$^{mut/fl}$, suggesting that the role of *Mdm2* haploinsufficiency in this context was p53-independent.

To investigate the gain of function of mutant p53 in our AML model, we compared the survival rates of *Mx-p53*$^{mut/fl}$ mice with those of *Mx-p53* $^{fl/fl}$ mice. The findings suggest that the mutant p53 does not exhibit a pronounced GOF effect beyond the loss of wild-type p53 tumor-suppressing functions (Figure 4H). The survival rates of *Mx-Mdm-p53*$^{mut/fl}$ mice were also similar to those of *Mx-p53*$^{mut/fl}$ mice, suggesting that in this AML model, *Mdm2* haploinsufficiency did not alter survival (Figure 4H). Further characterization of each BM sample by flow cytometry showed that the myeloid leukemia cells were mainly $CD11b^{+}Ly6G^{+}CD3^{-}$, while the erythroid leukemia cells were $CD34^{+}CD71^{+}$ (Figure 4I). We observed that p53 mutant cells (GFP+) were highly enriched in CD71 population whereas the population of $GFP^{neg}RFP^{neg}$ cells was predominantly Ter119 positive, indicating the expansion of mature erythroblasts (Figure 4I). To evaluate aneuploidy, which is a common feature of p53 mutant AML, we initially performed DNA content analysis. The population of GFP+ AML cells had higher DNA content compared to Tomato-positive p53 wild-type cells (Figure 4J). Further, whole exome sequencing analysis conducted on 16 AML samples with p53 mutations, and five control samples identified significant copy number alterations across various chromosomes (Figure 4K). Interestingly, we observed a recurrent microdeletion at 11q, and a deletion at 6q in 12 out of 16 (75%) AML samples, resembling the 7q deletion commonly found in human *TP53* mutant AML. The Integrative Genomics Viewer analysis of the sequencing data verified the presence of the *Trp53* R172H mutation in all 16 samples (Figure S5C).

Colony-forming analysis of BM cells from the *Mx-p53*$^{mut/fl}$ mice revealed granulocyte-macrophage (GM) colonies of GFP+ cells (Figure 4L), while erythroid leukemia cells showed BFU colonies (Figure 4M). In subsequent secondary transplant studies conducted in the syngeneic background or NSG mice, no leukemia developed even after a period of 6 months, despite the presence of detectable GFP and RFP cells in the recipients, suggesting that the p53 mutant leukemia cells may possess a more mature phenotype.

In conclusion, these data demonstrate the role of p53 mutations in the development of myeloid malignancies in adult HSCs, and that *Mdm2* haploinsufficiency in adult HSCs leads to the development of myeloid, but not lymphoid malignancies.

Mdm2 haploinsufficiency leads to myeloid-biased hematopoiesis

Both Mdm2 and p53 play crucial roles in the regulation of HSC differentiation and hematopoiesis.[28] To explore the role of Mdm2 in hematopoietic differentiation and myeloid-biased hematopoiesis, we focused on studying the hematopoietic phenotype of *Mdm2* haploinsufficient hematopoietic cells using *Vav-Cre;Mdm2*$^{fl/+}$*;mTmG* which will hereafter be referred to as *Vav-Mdm*$^{fl/+}$ mice. Evaluation of BM cells of *Vav-Mdm*$^{fl/+}$ mice at 10 days post-birth showed a reduction in cellularity compared

(L) Colony forming unit (CFU) assay shows granulocyte macrophage (GM) colonies under brightfield and fluorescence, highlighting the clonogenic ability of GFP+ cells, with Tomato+ cells showing no colony formation.
(M) Erythroid colony formation in AEL mice is shown through brightfield and direct fluorescence images, showing expansion of GFP+ colonies.

CellPress
OPEN ACCESS

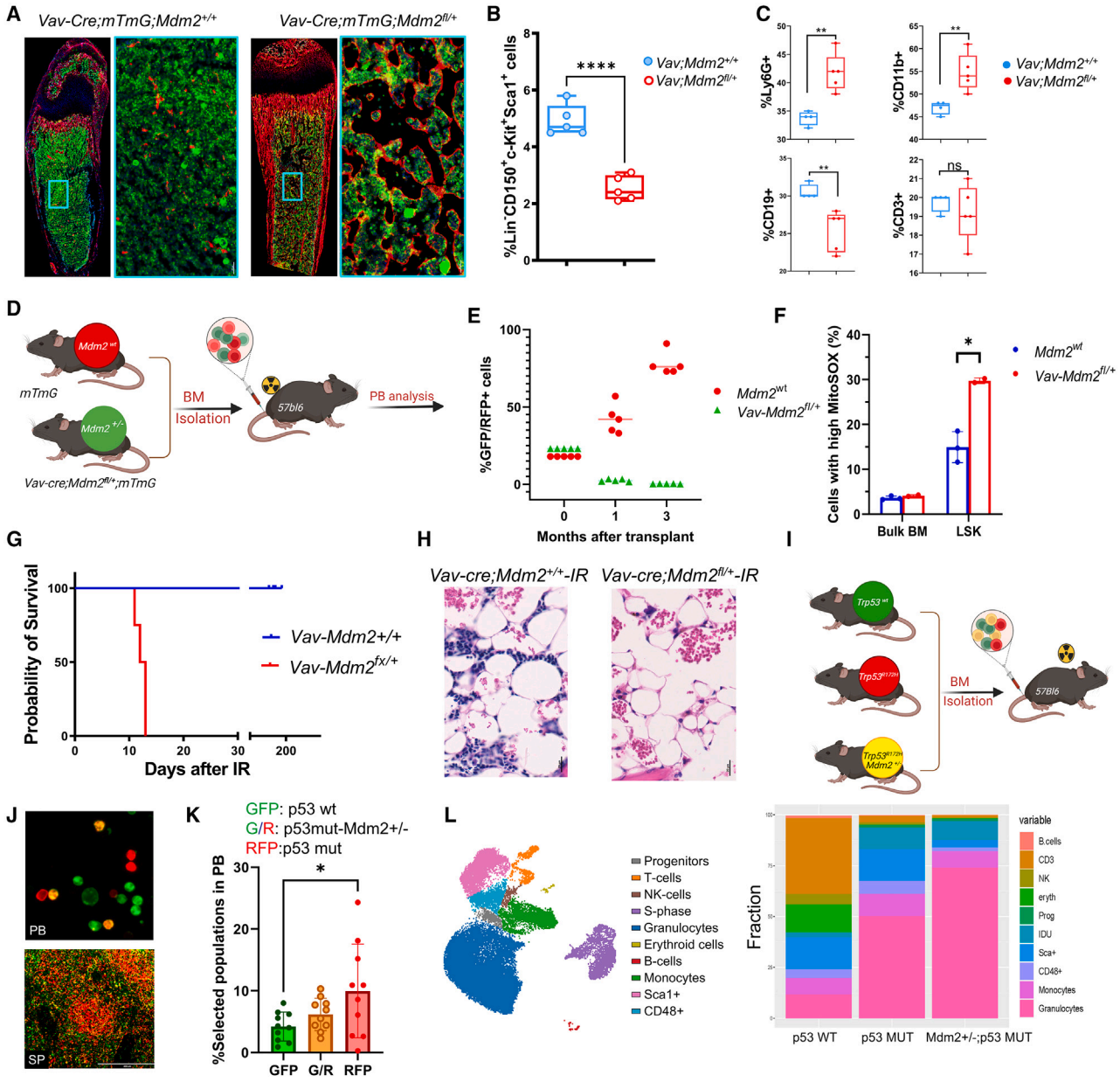

Figure 5. Myeloid-biased hematopoiesis resulting from *Mdm2* haploinsufficiency

(A) Direct fluorescence images of longitudinal sections of femurs derived from the indicated mice on postnatal day 10. GFP marks hematopoietic cells. A high-magnification view of the boxed region in the left panel is shown in the right panel.

(B) Quantification of the expression of the LSK population expression in the indicated mice. Each data point represents a measurement from an individual mouse; bars indicate means, and whiskers indicate SDs. ****$p < 0.0001$, $n = 5$.

(C) Expression of CD19, CD11b, Ly6G, and CD3 presented as percentages of total white blood cells (means ± SDs). **$p < 0.01$.

(D) Schematic depiction illustrating the experimental setup wherein BM cells from indicated donor mice were transplanted into recipient mice.

(E) Dot plot showing the percent of chimerism in indicated time points ($n = 5$).

(F) Quantification of ROS levels (means ± SDs) in indicated populations of BM isolated from indicated mice. *$p < 0.01$, $n = 3$.

(G) Kaplan-Meier analysis of the overall survival of indicated mice after irradiation.

(H) Representative histologic images of hematoxylin and eosin (H&E)-stained bone marrow sections from the indicated mice, taken 1 week after irradiation (IR).

(I) Schematic view of the transplant strategy. Mice were transplanted with a mixture of bone marrow cells-GFP (Trp53wt), Tomato (p53 mut), and GFP+Tomato (p53 mut, Mdm2 het) in equal proportions.

(J) Fluorescence images of peripheral blood (PB) and spleen show clone distribution.

(legend continued on next page)

to the control mice (Figure 5A). Furthermore, BM cells from *Vav-Mdm*$^{fl/+}$mice showed a significant reduction in LSK cells (Figure 5B), and a significant reduction in PB counts, coupled with an increase in the myeloid lineage and a decrease in the erythroid lineage (Figures S6A and S6B). Flow cytometry analysis of BM-derived cells indicated a significant increase in CD11b^{+} and Ly6G $^{+}$ cell populations in *Vav-Mdm*$^{fl/+}$mice, suggesting myeloid-biased hematopoiesis (Figure 5C).

To investigate the effects of *Mdm2* haploinsufficiency on hematopoietic stem/progenitor cells, we conducted a comprehensive analysis using both *in vitro* (colony formation and serial replating assays) and *in vivo* (competitive repopulation) functional assays. LSK cells were isolated from *Vav;Mdm*$^{fl/+}$ and control mice to evaluate their colony-forming capabilities. Notably, the *Vav;Mdm*$^{fl/+}$ mice demonstrated small colonies and increase in colony-forming unit-granulocyte-macrophage (CFU-GM) progenitors, and a significant reduction in colony formation in serial replating assays (Figures S6C–S6E). These findings suggest that *Mdm2* haploinsufficiency specifically impacts the formation of GM progenitors, potentially leading to alterations in myeloid lineage development.

Long-term repopulation assay in irradiated recipient mice over 3 months was performed to evaluate the HSC self-renewal and differentiation potential. Equal numbers of BM cells from *Vav;Mdm*$^{fl/+}$ (GFP+) and control *mTmG* mice (Tomato+) were transplanted into lethally irradiated recipients and monitored to assess engraftment and reconstitution ability (Figure 5D). A significant decrease in engraftment and multilineage reconstitution ability was observed in *Vav;Mdm*$^{fl/+}$ compared with control mice (Figure 5E). Flow cytometry analysis of BM cells derived from *Vav-Mdm2*$^{fl/+}$ mice further revealed higher levels of reactive oxygen species (ROS) in the LSK population (Figure 5F), suggesting that *Mdm2* haploinsufficiency may contribute to increased oxidative stress and impaired HSC function. In addition, *Vav;Mdm*$^{fl/+}$ mice displayed heightened radiosensitivity and lethal hematopoietic failure following irradiation (Figure 5G). Histological examination of the BM in *Vav;Mdm*$^{fl/+}$ mice after irradiation revealed a broad loss of hematopoietic lineage, indicating the essential role of Mdm2 levels in maintaining hematopoietic integrity after DNA damage (Figure 5H). These data indicate that *Mdm2* haploinsufficiency in *Vav-Mdm2*$^{fl/+}$ mice leads to impaired HSC function and maintenance in response to DNA damage stress.

Next, we examined if the observed phenotype in *Vav;Mdm*$^{fl/+}$ mice was p53 dependent. Deletion of p53 in *Vav;Mdm*$^{fl/+}$ mice rescued the LSK population and improved colony formation, showing that p53 loss can counteract some defects in *Mdm2*$^{+/-}$ HSCs (Figures S6F and S6G). To evaluate the phenotype *in vivo*, we conducted a competitive transplant experiment using BM cells from *Vav;mTmG* (p53WT-green), *Vav;Rosa*$^{Lsl\text{-}TdTomato}$*;p53*$^{mut/fl}$ (p53-mutant, red) and *Vav;Rosa*$^{Lsl\text{-}TdTomato}$*;mTmG;Mdm-p53*$^{mut/fl}$ (p53-mutant-*Mdm2*$^{+/-}$, yellow) cells (Figure 5I). Six weeks post-transplant, these transplanted populations were detectable in the PB and spleen (Figure 5J). Notably, the population of p53 mutant cells was significantly higher than the other groups (Figure 5K). To further investigate the impact of *Mdm2* haploinsufficiency on the hematopoietic hierarchies, we performed multiplexed CyTOF analysis of the BM in indicated mice. We employed unsupervised analysis to identify distinct lineages in the BM and assessed the impact of each genetic modification on cell composition. Notably, our analysis revealed the preferential expansion of granulocytic lineages in p53-mutant-*Mdm2*$^{+/-}$ BM cells (Figure 5L). This expansion occurred at the expense of lymphoid lineage and other lineages, indicating a significant skewing of BM differentiation trajectories toward myeloid differentiation. This result further supports our findings that the *Mdm2* haploinsufficiency promotes differentiation toward the myeloid lineage, and that this effect is p53-independent.

Our collective findings suggest that *Mdm2* haploinsufficiency leads to impaired HSC function, including myeloid-biased differentiation, engraftment defect, and increased oxidative stress. Moreover, these effects on differentiation appear to be independent of p53 function.

Mechanisms of *Mdm2* haploinsufficiency in myeloid-biased hematopoiesis

To investigate how *Mdm2* haploinsufficiency results in myeloid-biased hematopoiesis, we conducted RNA sequencing (RNA-seq) on Lin-ckit+ (LK) cells isolated from the BM of adult *Vav;Mdm*^{Wt}, *Vav;Mdm*$^{fl/+}$, and *Vav;Mdm*$^{fl/+}$*;p53* $^{fl/fl}$ mice (Figure 6A). We observed 2,961 upregulated and 1,648 downregulated genes (±1.5-fold, false discovery rate [FDR] = 0.05) in *Vav;Mdm*$^{fl/+}$ compared with *Vav;Mdm*^{Wt} mice (Figure 6B). Surprisingly, the gene expression signature of LK cells isolated from *Vav;Mdm*$^{fl/+}$*;p53* $^{fl/fl}$ mice was very similar to that of *Vav;Mdm*$^{fl/+}$ mice (Figure 6C), indicating that the gene signature associated with *Mdm2* haploinsufficiency was independent of p53. Deletion of *Trp53* in *Vav;Mdm*$^{fl/+}$ mice only led to upregulation of 20 genes and downregulation of 62 genes (Figure 6C). The transcript level of *Mdm2* was reduced by 50% in *Vav;Mdm2*$^{fl/+}$ and *Vav;Mdm*$^{fl/+}$*;p53* $^{fl/fl}$ mice, implying that *Mdm2* copy numbers, and not p53 levels, determine its expression levels (Figure 6D).

Ingenuity pathway analysis (IPA) of differential gene expression revealed significant downregulation of cholesterol biosynthesis and the mevalonate pathway ($-\log2\ p = 20$) in *Vav;Mdm*$^{fl/+}$ mice compared with *Vav;Mdm*^{Wt} mice (Figure 6E). In addition, TREM1 signaling, Th1 and Th2 activation, and IL8 signaling, were significantly enriched in the downregulated gene set (Figure 6E). Strikingly, 85% of genes involved in cholesterol biosynthesis, including seven encoding enzymes within the mevalonate pathway (*Hmgcr*, *Mvk*, *Mvd*, *Fdps*, *Sqle*, *Lss*, *Dhcr7*), were downregulated in *Vav;Mdm*$^{fl/+}$ mice (Figure 6F). Importantly, deletion of *Trp53* in

(K) The bar plot shows cell population frequencies in peripheral blood 4 weeks after transplant, identified by flow cytometry. Each data point represents a measurement from an individual mouse; bars indicate means.*$p < 0.01$.

(L) UMAP visualization depicting distinct cell subsets identified in pooled BM samples cells-GFP (Trp53wt), Tomato (p53 mut), and GFP+Tomato (p53 mut, Mdm2 het). Different cell lineages are color-coded for easy identification. The stacked bar plots provide a summary of subset frequencies across the specified genotypes.

CellPress
OPEN ACCESS

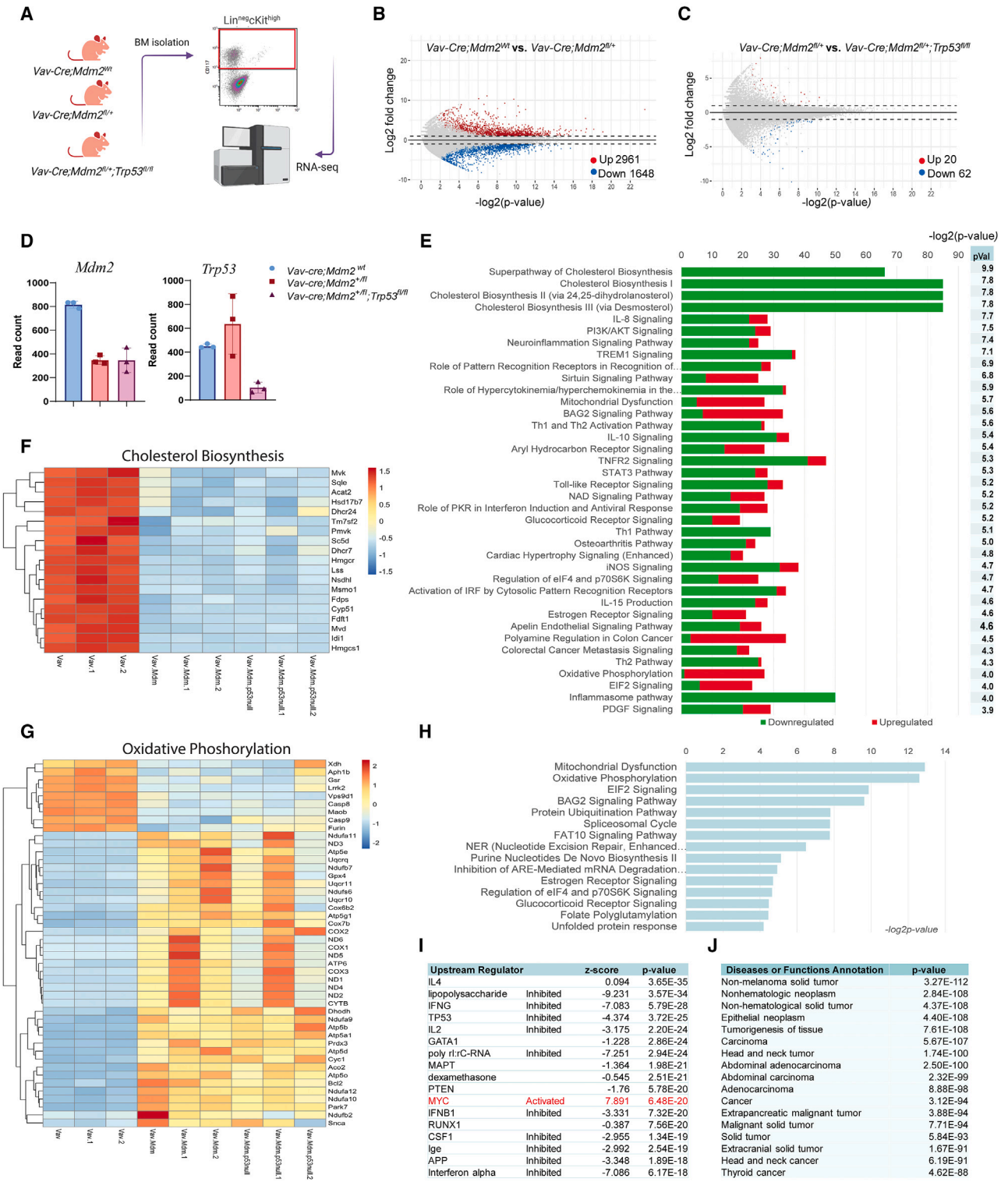

I

Upstream Regulator		z-score	p-value
IL4		0.094	3.65E-35
lipopolysaccharide	Inhibited	-9.231	3.57E-34
IFNG	Inhibited	-7.083	5.79E-28
TP53	Inhibited	-4.374	3.72E-25
IL2	Inhibited	-3.175	2.20E-24
GATA1		-1.228	2.86E-24
poly rI:rC-RNA	Inhibited	-7.251	2.94E-24
MAPT		-1.364	1.98E-21
dexamethasone		-0.545	2.51E-21
PTEN		-1.76	5.78E-20
MYC	Activated	7.891	6.48E-20
IFNB1	Inhibited	-3.331	7.32E-20
RUNX1		-0.387	7.56E-20
CSF1	Inhibited	-2.955	1.34E-19
Ige	Inhibited	-2.992	2.54E-19
APP	Inhibited	-3.348	1.89E-18
Interferon alpha	Inhibited	-7.086	6.17E-18

J

Diseases or Functions Annotation	p-value
Non-melanoma solid tumor	3.27E-112
Nonhematologic neoplasm	2.84E-108
Non-hematological solid tumor	4.37E-108
Epithelial neoplasm	4.40E-108
Tumorigenesis of tissue	7.61E-108
Carcinoma	5.67E-107
Head and neck tumor	1.74E-100
Abdominal adenocarcinoma	2.50E-100
Abdominal carcinoma	2.32E-99
Adenocarcinoma	8.88E-98
Cancer	3.12E-94
Extrapancreatic malignant tumor	3.88E-94
Malignant solid tumor	7.71E-94
Solid tumor	5.84E-93
Extracranial solid tumor	1.67E-91
Head and neck cancer	6.19E-91
Thyroid cancer	4.62E-88

Figure 6. *Mdm2* haploinsufficiency represses the mevalonate pathway independently of p53

(A) Schematic representation of experimental design. The total RNA extracted from Lin$^-$ cKit$^+$ cells sorted from the indicated mice were analyzed by RNA sequencing.

(B and C) Mean-average plots of Log2 mean expression vs. Log2 fold change in mice with the indicated genotypes. Red dots indicate genes that were upregulated (Log2FC > 1 and $p < 0.05$). Blue dots indicate genes that were downregulated (Log2FC < −1 and $p < 0.05$).

(legend continued on next page)

Vav;Mdm2$^{fl/+}$ mice (*Vav;Mdm2*$^{fl/+}$;*p53* $^{fl/fl}$) did not change this signature, indicating that the mevalonate pathway downregulation was p53 independent. Furthermore, the gene signature associated with oxidative phosphorylation (OxPhos) was significantly upregulated in *Vav;Mdm2*$^{fl/+}$ mice independent of p53 (Figures 6G and 6H), suggesting a potential compensatory mitochondrial stress response in HSCs with *Mdm2* haploinsufficiency.

The key regulatory factors influencing the observed gene expression in *Vav;Mdm2*$^{fl/+}$ mice (lipopolysaccharide, IFNG, TP53, and IL2) were all downregulated (Figure 6I). Notably, the expression of *Myc* and its associated signature was upregulated in *Vav;Mdm2*$^{fl/+}$ mice (Figure 6I). IPA also showed a strong correlation between the *Mdm2* signature with the gene signature observed in non-hematological malignancies (Figure 6J), suggesting that the *Mdm2* haploinsufficiency-associated gene signature is highly enriched in cancers. In summary, these data demonstrate that *Mdm2* haploinsufficiency leads to significant changes in gene expression in HSCs, particularly in the downregulation of cholesterol biosynthesis and the upregulation of oxidative phosphorylation. These changes appear to be independent of p53, as deletion of *Trp53* did not alter the gene signature associated with *Mdm2* haploinsufficiency.

Disruption of the mevalonate pathway by *Mdm2* haploinsufficiency, and synergistic induction of apoptosis through combined inhibition of mevalonate pathway and Mdm2

The mevalonate pathway, regulated by Srebp, is responsible for synthesizing cholesterol and isoprenoids. Statin drugs inhibit the mevalonate pathway, affecting CoQ production and blocking squalene monooxygenase (Sqle)-mediated cholesterol synthesis (Figure 7A). To elucidate the effects of *Mdm2* haploinsufficiency on the mevalonate pathway and its impact on hematopoietic differentiation, we compared the levels of p21, known to regulated HSC differentiation,[29] p53, and Sqle in *Vav-Mdm2*$^{fl/+}$ mice and control mice. The *Vav-Mdm2*$^{fl/+}$ mice exhibited a notable reduction in Sqle protein (Figure 7B). In *Mdm2* haploinsufficient mice, p53 levels were comparable to those in wild-type mice, yet p21 levels were elevated compared with the control mice (Figures 7B and 7C). Analysis of BM cells derived from irradiated mice revealed an upregulation of p21 and downregulation of Srebp2 precursor levels in *Vav-Mdm2*$^{fl/+}$ mice (Figure 7D). The observed decrease in Srebp2 expression further supports the idea that *Mdm2* haploinsufficiency may downregulate the mevalonate pathway via Srebp2 levels.

To assess the RNA-seq findings that suggested Eif2 signaling activation in *Mdm2* haploinsufficient HSC/progenitor cells (Figure 6H), we conducted western blot analysis on spleen cells from *Vav-Mdm2*$^{fl/+}$ and control mice. This analysis revealed higher levels of *p*-Eif2a in the *Vav-Mdm2*$^{fl/+}$ mice, suggesting that *Mdm2* haploinsufficiency may activate the integrated stress response (ISR) pathway (Figures S7A and S7B). To evaluate if inhibition of the mevalonate pathway may play a role, K562 cells were treated with the RORγ inhibitor XY018, which is known to decrease cholesterol biosynthesis rate without affecting host cholesterol homeostasis.[30] This treatment led to significant decreases in Hmgcs and Sqle levels and an increase in *p*-Eif2a levels, indicating that cholesterol metabolism inhibition might trigger ISR activation (Figure 7E). However, ISR activation through Thapsigargin resulted in increased Hmgcs and Sqle levels, pointing to a complex regulatory interaction between these pathways (Figure S7C).

Next, we investigated the impact of statin-mediated inhibition of cholesterol biosynthesis on myeloid differentiation. LSK cells isolated from wild-type mice were treated with atorvastatin in colony-forming cultures, and showed a significant increase in myeloid differentiation indicated by CD11b^{+} cells (t test, p = 0.0001) (Figure 7F), suggesting the involvement of the mevalonate pathway in myeloid differentiation. Furthermore, treating p53-null HL60 cells with atorvastatin promoted myeloid differentiation (Figure 7G), accompanied by a dose-dependent inhibition of cell proliferation (Figure 7H). These data further support the contribution of the mevalonate pathway in myeloid differentiation.

To determine whether atorvastatin could synergize with the MDM2 inhibitor (MDM2i) nutlin3a (N3a) to promote cell apoptosis in AML, we treated three AML cell lines with varying concentrations of atorvastatin as previously described,[31] nutlin3a, or a combination of both. We also examined the effects of atorvastatin and nutlin3a in the presence and absence of CoQ. All three cell lines were relatively sensitive to both nutlin3a and atorvastatin, but the combination was synergistic in all three cell lines (Figures 7I–7K and S7D–S7F). Notably, CoQ treatment reduced apoptotic cell death, especially in the atorvastatin/nutlin3a combination group, suggesting that inhibiting the mevalonate pathway may enhance MDM2i-mediated oxidative stress by depleting CoQ. Additionally, we measured lipid peroxidation and found that the atorvastatin/nutlin3a combination increased lipid peroxidation (Figure 7L). Together, these results reveal a role for the mevalonate pathway in myeloid differentiation and suggest that a combination of statins and MDM2 inhibitors is potentially effective in the treatment of AML.

(D) Bar graphs representing the average read counts of genes in the indicated mice (mean ± SD).
(E) Ingenuity pathway analysis (IPA) of differentially expressed genes (DEGs) representing the percentage of significant DEGs out of the total genes in each pathway that were downregulated (green) or upregulated (red) in *Mdm2*-haploinsufficient hematopoietic progenitors, ranked by *p* values (*p*Val).
(F) Heatmap representing changes in gene expression of the cholesterol biosynthesis pathway in *Vav-Cre;Mdm2*$^{fl/+}$ mice compared with *Vav-Cre;Mdm2*$^{+/+}$mice and *Vav-Cre;Mdm2*$^{fl/+}$;*Trp53* $^{fl/fl}$.
(G) Heatmap representing changes in gene expression of the oxidative phosphorylation (OxPhos) pathway.
(H) IPA analysis of upregulated genes in *Mdm2*-haploinsufficient mice.
(I) IPA upstream regulator analysis of DEGs in *Vav-Cre;Mdm2*$^{+/fl}$ vs. *Vav-Cre;Mdm2*$^{+/+}$ mice showing inhibition of indicated upstream regulators and activation of Myc (red).
(J) IPA disease or functions annotation of DEGs between *Vav-Cre;Mdm2*$^{+/fl}$ vs. *Vav-Cre;Mdm2*$^{+/+}$ mice.

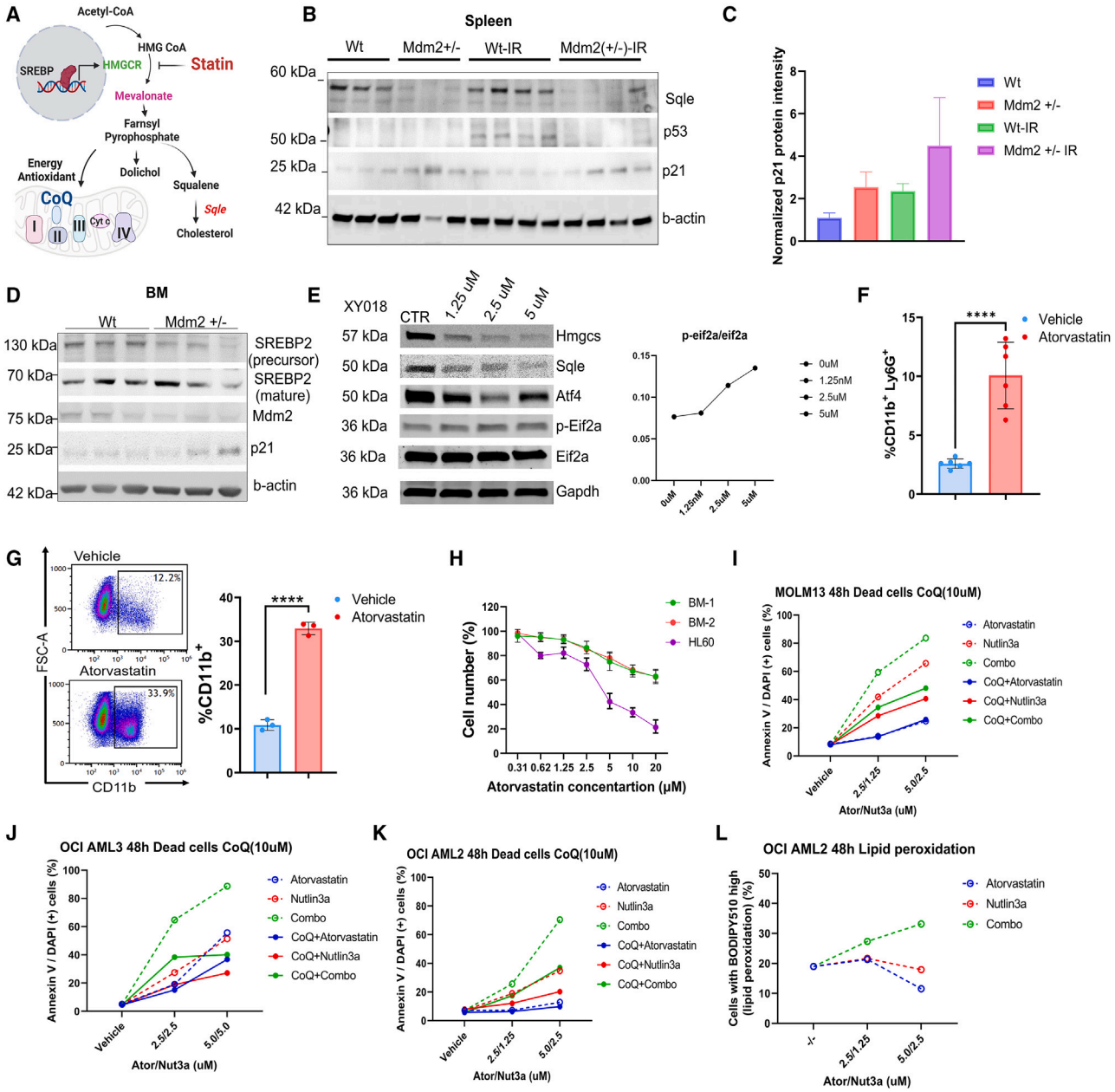

Figure 7. Inhibition of mevalonate metabolism induces myeloid differentiation and synergizes with MDM2i to induce apoptosis in AML cells

(A) Schematic representation of the mevalonate pathway. The mevalonate pathway, regulated by SREBP, is responsible for synthesizing cholesterol and isoprenoids. Statin drugs inhibit SREBP activation, affecting CoQ production and blocking Sqle-mediated cholesterol synthesis.

(B) Western blot analysis of Sqle, p53, p21, and b-actin levels in spleen cells derived from *Vav-Cre;Mdm2*$^{+/+}$ and *Vav-Cre;Mdm2*$^{+/fl}$, before and after irradiation (6 Gy). The figure displays bands corresponding to the molecular weights of the respective proteins.

(C) Quantification of p21 protein levels in (B), normalized to beta-actin. Bar graphs represent the mean protein expression level relative to the control, with error bars indicating the standard error of the mean (SEM) based on two separate blots.

(D) Western blot analysis of SREBP, Mdm2, p21, and β-actin protein levels in bone marrow cells derived from *Vav-Cre;Mdm2*$^{+/+}$ and *Vav-Cre;Mdm2*$^{+/fl}$, after irradiation (6 Gy). The bands at the corresponding molecular weights are displayed.

(E) Western blot analysis of K562 cells treated with indicated concentrations of XY018. The figure displays bands corresponding to the molecular weights of the respective proteins. The normalized levels of phospho-eIF2α are shown on the right.

(F) Quantification of myeloid cells (CD11b^{+}) in CFU culture treated with atorvastatin, displaying means ± SDs. Each data point represents a measurement from an individual mouse. ****$p < 0.0001$.

(G) Representative flow cytometry plot and quantification of the frequency of CD11b^{+} in HL60 cells after 48 h treatment with atorvastatin. ****$p < 0.0001$.

(legend continued on next page)

DISCUSSION

AML remains a challenging disease with poor outcomes, particularly in cases involving *TP53* mutations, yet the precise molecular mechanisms underlying the disease remain elusive, primarily due to the lack of suitable mouse models. The *Trp53*^{R172H} mutation in mice and its human equivalent, the R175H allele, contribute to abnormal self-renewal and enhanced cell proliferation in AML.[17] Our study, utilizing an inducible *Trp53*^{R172H} mouse model and *Mdm2* heterozygous deletion models, reveals new insights into the cooperative effects of *Trp53* mutations and *Mdm2* haploinsufficiency on clonal hematopoiesis and myeloid lineage development. While Mdm2 has previously been associated with cell-cycle progression independently of p53,[32] our findings uncover an additional p53-independent role for Mdm2 in regulating the mevalonate pathway and cellular stress response, which influence myeloid differentiation in hematopoietic cells.

Mdm2 plays a critical role in regulating cell fate decisions within the hematopoietic system by modulating p53 levels, thereby balancing self-renewal and differentiation in HSCs.[33,34] Our investigation into the hematopoietic defects observed in conditional *Mdm2* haploinsufficient mice revealed that, contrary to our expectation, p53 levels did not increase in BM cells of these mice, even after irradiation-induced DNA damage, suggesting that the phenotype of *Mdm2* haploinsufficiency in BM cells is not solely attributed to increased p53 activity. However, the upregulation of p21, a p53 target gene, suggests a potential p53-independent mechanism, consistent with previous reports of MDM2 inhibition leading to p53-independent increases in p21 levels.[35] Furthermore, *Mdm2* haploinsufficiency still promoted granulocytic differentiation even in the absence of p53, aligning with previous reports of its p53-independent role in differentiation,[36] such as the induction of granulocytic differentiation in p53 null HL-60 cells by nulin-3a.[37] In the context of hematologic malignancies, the presence of *MDM2*(SNP309) was found as a biomarker associated with worse clinical outcomes in AML patients.[38]

Recent studies underscore the significance of HSC age in determining susceptibility to transformation and the type of malignancy that arises.[39,40] Aging HSCs are associated with myeloid-biased hematopoiesis, linked to myeloid malignancies like AML.[41,42] The observed activation of ISR pathway in *Mdm2* haploinsufficient BM cells suggest an increased state of cellular stress, potentially accelerating the aging process in HSCs. Furthermore, *Mdm2* haploinsufficiency compromises the self-renewal and differentiation potential of HSCs, ultimately leading to a skewing toward myeloid lineage. Therefore, further investigations into how ISR activation influences HSC aging in the context of *Mdm2* haploinsufficiency are essential. These studies provide invaluable insights into the mechanisms underlying age-related hematopoietic disorders.

The genetic mouse model of *Mdm2* haploinsufficiency offers insights into the p53-independent role of Mdm2 in the maintenance and differentiation of HSCs. Pharmacological inhibition of MDM2, unleashing the pro-apoptotic effects of p53, holds promise as a treatment approach for malignancies with intact *TP53*.[43,44] However, concerns arise regarding the possible selection of *TP53*-mutant subclones with GOF activities.[45,46] Previous research, including our own, has indicated that MDM2 inhibition may inadvertently promote the expansion of *TP53*-mutant clones.[47–49] Our findings, demonstrating no significant difference between p53 mutant and p53 null groups, suggest that mutant p53 in our model lacks pronounced GOF effects. These results align with recent studies in the field,[50,51] further supporting the notion that the mutant p53 does not exhibit enhanced oncogenic properties beyond loss of wild-type p53 function.

Mdm2 haploinsufficiency was previously shown to alter the tumor spectrum in p53-null mice, showing lower incidence of lymphoma.[52,53] Importantly, our data clarify the role of *Mdm2* haploinsufficiency in leukemogenesis, demonstrating that *Mdm2* haploinsufficiency can promote granulocytic differentiation of p53 null BM cells partly through inhibition of the mevalonate pathway. While our findings highlight the significance of *Mdm2* haploinsufficiency in myeloid-biased hematopoiesis, its specific role in the transition from clonal hematopoiesis to AML warrants further investigation. We propose that dysregulation of Mdm2 and p53 pathways may contribute to clonal expansion and genomic instability, facilitating the progression from pre-leukemic states to overt AML. However, elucidating the precise mechanisms underlying this transition requires additional research.

Limitations of the study

Our study sheds light on the interaction between *Mdm2* haploinsufficiency and mutant p53 in AML development. However, given the heterogeneity of AML in humans, our findings may primarily apply to specific AML subsets, especially those with p53 mutations and *MDM2* LOH, hence our results might not extend to all AML patient scenarios. Moreover, while we provide valuable insights into the roles of Mdm2 and mutant p53 in the context of animal models, especially regarding myeloid-biased hematopoiesis, we recognize that our study does not fully elucidate the mechanisms of leukemogenesis. Alternative mechanisms and the direct translation of these findings to human disease requires further research.

STAR★METHODS

Detailed methods are provided in the online version of this paper and include the following:

- KEY RESOURCES TABLE
- RESOURCE AVAILABILITY
  - Lead contact
  - Materials availability
  - Data and code availability

(H) Percentage of live cells in indicated cells treated with different concentration of atorvastatin. Error bars indicate the standard error of the mean (SEM), representing the variability within the experimental replicates.
(I–K) Percentage of dead cells defined as Annexin V/DAPI(+) cells in indicated cell lines treated with indicated compounds and concentrations.
(L) Percentage of cells with high peroxidation index treated with indicated compounds.

SUPPLEMENTAL INFORMATION

Supplemental information can be found online at https://doi.org/10.1016/j.xcrm.2024.101558.

ACKNOWLEDGMENTS

We express our gratitude to the staff of the Research Animal Support Facility and to Nalini Patel, Nguyen Nguyen, and Nicole R. Vaughn in the Flow Cytometry and Cellular Imaging Core (supported by NIH grant P30 CA016672). Special thanks go to Dr. Gigi Lozano for providing *Trp53*^{wmR172H} mice and to Sean Post for critically reading the manuscript. We extend our appreciation to Mahesh Basyal, Edward Ayoub, Erika Thompson, Sunita Patterson, Sara McCracken, Sherry Pierce, and Jairo Matthews for their invaluable assistance. Additionally, we would like to thank Dr. Arnold J. Levine for insightful discussions. This research was made possible through funding from the Paul and Mary Haas Chair in Genetics (to M.A.), a CPRIT MIRA (to M.A.), The Ladies Leukemia League research grant (to R.P.), NIH SPORE Career Enhancement Award (to R.P.), and the University of Texas MD Anderson Cancer Center MDS/AML Moon Shot (to M.A.). T.L. and P.V.L. are supported by the Francis Crick Institute, which receives core funding from Cancer Research UK (CC2008), the UK Medical Research Council (CC2008), and the Wellcome Trust (CC2008). P.V.L. is a CPRIT Scholar in Cancer Research and acknowledges CPRIT grant support (RR210006).

AUTHOR CONTRIBUTIONS

Conceptualization: R.P. and M.A. Methodology: R.P. and M.G. Software: B.L., M.M., T.L., and P.V.L. Investigation: R.P., R.H.M., H.A., L.O., S.K., R.Z., J.D.K., N.B., and M.G. Resources: M.A. and R.P. Writing – original draft: R.P. Writing – review & editing: M.A. Supervision: P.V.L. and M.A. Project administration: R.P. Funding acquisition: R.P. and M.A.

DECLARATION OF INTERESTS

The authors declare no potential conflicts of interest.

Received: August 16, 2023
Revised: February 18, 2024
Accepted: April 17, 2024
Published: May 10, 2024

REFERENCES

1. Daver, N.G., Maiti, A., Kadia, T.M., Vyas, P., Majeti, R., Wei, A.H., Garcia-Manero, G., Craddock, C., Sallman, D.A., and Kantarjian, H.M. (2022). TP53-Mutated Myelodysplastic Syndrome and Acute Myeloid Leukemia: Biology, Current Therapy, and Future Directions. Cancer Discov. *12*, 2516–2529. https://doi.org/10.1158/2159-8290.CD-22-0332.
2. Jones, S.N., Roe, A.E., Donehower, L.A., and Bradley, A. (1995). Rescue of embryonic lethality in Mdm2-deficient mice by absence of p53. Nature *378*, 206–208. https://doi.org/10.1038/378206a0.
3. Montes de Oca Luna, R., Wagner, D.S., and Lozano, G. (1995). Rescue of early embryonic lethality in mdm2-deficient mice by deletion of p53. Nature *378*, 203–206. https://doi.org/10.1038/378203a0.
4. Adams, C.M., Mitra, R., Xiao, Y., Michener, P., Palazzo, J., Chao, A., Gour, J., Cassel, J., Salvino, J.M., and Eischen, C.M. (2023). Targeted MDM2 Degradation Reveals a New Vulnerability for p53-Inactivated Triple-Negative Breast Cancer. Cancer Discov. *13*, 1210–1229. https://doi.org/10.1158/2159-8290.CD-22-1131.
5. Levine, A.J. (1997). p53, the cellular gatekeeper for growth and division. Cell *88*, 323–331. https://doi.org/10.1016/s0092-8674(00)81871-1.
6. Oliner, J.D., Kinzler, K.W., Meltzer, P.S., George, D.L., and Vogelstein, B. (1992). Amplification of a gene encoding a p53-associated protein in human sarcomas. Nature *358*, 80–83. https://doi.org/10.1038/358080a0.
7. Haupt, Y., Maya, R., Kazaz, A., and Oren, M. (1997). Mdm2 promotes the rapid degradation of p53. Nature *387*, 296–299. https://doi.org/10.1038/387296a0.
8. Kubbutat, M.H., Jones, S.N., and Vousden, K.H. (1997). Regulation of p53 stability by Mdm2. Nature *387*, 299–303. https://doi.org/10.1038/387299a0.
9. Honda, R., Tanaka, H., and Yasuda, H. (1997). Oncoprotein MDM2 is a ubiquitin ligase E3 for tumor suppressor p53. FEBS Lett. *420*, 25–27. https://doi.org/10.1016/s0014-5793(97)01480-4.
10. Swaminathan, M., Bannon, S.A., Routbort, M., Naqvi, K., Kadia, T.M., Takahashi, K., Alvarado, Y., Ravandi-Kashani, F., Patel, K.P., Champlin, R., et al. (2019). Hematologic malignancies and Li-Fraumeni syndrome. Cold Spring Harb. Mol. Case Stud. *5*, a003210. https://doi.org/10.1101/mcs.a003210.
11. Donehower, L.A., and Lozano, G. (2009). 20 years studying p53 functions in genetically engineered mice. Nat. Rev. Cancer *9*, 831–841. https://doi.org/10.1038/nrc2731.
12. ICGC/TCGA Pan-Cancer Analysis of Whole Genomes Consortium (2020). Pan-cancer analysis of whole genomes. Nature *578*, 82–93. https://doi.org/10.1038/s41586-020-1969-6.
13. Feeley, K.P., Adams, C.M., Mitra, R., and Eischen, C.M. (2017). Mdm2 Is Required for Survival and Growth of p53-Deficient Cancer Cells. Cancer Res. *77*, 3823–3833. https://doi.org/10.1158/0008-5472.CAN-17-0809.
14. Ghandi, M., Huang, F.W., Jané-Valbuena, J., Kryukov, G.V., Lo, C.C., McDonald, E.R., 3rd, Barretina, J., Gelfand, E.T., Bielski, C.M., Li, H., et al. (2019). Next-generation characterization of the Cancer Cell Line Encyclopedia. Nature *569*, 503–508. https://doi.org/10.1038/s41586-019-1186-3.
15. Bond, G.L., Hu, W., Bond, E.E., Robins, H., Lutzker, S.G., Arva, N.C., Bargonetti, J., Bartel, F., Taubert, H., Wuerl, P., et al. (2004). A single nucleotide polymorphism in the MDM2 promoter attenuates the p53 tumor suppressor pathway and accelerates tumor formation in humans. Cell *119*, 591–602. https://doi.org/10.1016/j.cell.2004.11.022.
16. Olive, K.P., Tuveson, D.A., Ruhe, Z.C., Yin, B., Willis, N.A., Bronson, R.T., Crowley, D., and Jacks, T. (2004). Mutant p53 gain of function in two mouse models of Li-Fraumeni syndrome. Cell *119*, 847–860. https://doi.org/10.1016/j.cell.2004.11.004.
17. Loizou, E., Banito, A., Livshits, G., Ho, Y.J., Koche, R.P., Sánchez-Rivera, F.J., Mayle, A., Chen, C.C., Kinalis, S., Bagger, F.O., et al. (2019). A Gain-of-Function p53-Mutant Oncogene Promotes Cell Fate Plasticity and Myeloid Leukemia through the Pluripotency Factor FOXH1. Cancer Discov. *9*, 962–979. https://doi.org/10.1158/2159-8290.CD-18-1391.
18. Hill, R., Song, Y., Cardiff, R.D., and Van Dyke, T. (2005). Selective evolution of stromal mesenchyme with p53 loss in response to epithelial tumorigenesis. Cell *123*, 1001–1011. https://doi.org/10.1016/j.cell.2005.09.030.
19. Pourebrahim, R., Zhang, Y., Liu, B., Gao, R., Xiong, S., Lin, P.P., McArthur, M.J., Ostrowski, M.C., and Lozano, G. (2017). Integrative genome analysis

of somatic p53 mutant osteosarcomas identifies Ets2-dependent regulation of small nucleolar RNAs by mutant p53 protein. Genes Dev. *31*, 1847–1857. https://doi.org/10.1101/gad.304972.117.

20. Zhang, Y., Xiong, S., Liu, B., Pant, V., Celii, F., Chau, G., Elizondo-Fraire, A.C., Yang, P., You, M.J., El-Naggar, A.K., et al. (2018). Somatic Trp53 mutations differentially drive breast cancer and evolution of metastases. Nat. Commun. *9*, 3953. https://doi.org/10.1038/s41467-018-06146-9.
21. Marino, S., Vooijs, M., van Der Gulden, H., Jonkers, J., and Berns, A. (2000). Induction of medulloblastomas in p53-null mutant mice by somatic inactivation of Rb in the external granular layer cells of the cerebellum. Genes Dev. *14*, 994–1004.
22. Grier, J.D., Yan, W., and Lozano, G. (2002). Conditional allele of mdm2 which encodes a p53 inhibitor. Genesis *32*, 145–147.
23. Lang, G.A., Iwakuma, T., Suh, Y.A., Liu, G., Rao, V.A., Parant, J.M., Valentin-Vega, Y.A., Terzian, T., Caldwell, L.C., Strong, L.C., et al. (2004). Gain of function of a p53 hot spot mutation in a mouse model of Li-Fraumeni syndrome. Cell *119*, 861–872. https://doi.org/10.1016/j.cell.2004.11.006.
24. Jacks, T., Remington, L., Williams, B.O., Schmitt, E.M., Halachmi, S., Bronson, R.T., and Weinberg, R.A. (1994). Tumor spectrum analysis in p53-mutant mice. Curr. Biol. *4*, 1–7. https://doi.org/10.1016/s0960-9822(00)00002-6.
25. Harvey, M., McArthur, M.J., Montgomery, C.A., Jr., Butel, J.S., Bradley, A., and Donehower, L.A. (1993). Spontaneous and carcinogen-induced tumorigenesis in p53-deficient mice. Nat. Genet. *5*, 225–229. https://doi.org/10.1038/ng1193-225.
26. Velasco-Hernandez, T., Säwén, P., Bryder, D., and Cammenga, J. (2016). Potential Pitfalls of the Mx1-Cre System: Implications for Experimental Modeling of Normal and Malignant Hematopoiesis. Stem Cell Rep. *7*, 11–18. https://doi.org/10.1016/j.stemcr.2016.06.002.
27. Kogan, S.C., Ward, J.M., Anver, M.R., Berman, J.J., Brayton, C., Cardiff, R.D., Carter, J.S., de Coronado, S., Downing, J.R., Fredrickson, T.N., et al. (2002). Bethesda proposals for classification of nonlymphoid hematopoietic neoplasms in mice. Blood *100*, 238–245. https://doi.org/10.1182/blood.v100.1.238.
28. Wu, D., and Prives, C. (2018). Relevance of the p53-MDM2 axis to aging. Cell Death Differ. *25*, 169–179. https://doi.org/10.1038/cdd.2017.187.
29. Cheng, T., Rodrigues, N., Shen, H., Yang, Y., Dombkowski, D., Sykes, M., and Scadden, D.T. (2000). Hematopoietic stem cell quiescence maintained by p21cip1/waf1. Science *287*, 1804–1808. https://doi.org/10.1126/science.287.5459.1804.
30. Cai, D., Wang, J., Gao, B., Li, J., Wu, F., Zou, J.X., Xu, J., Jiang, Y., Zou, H., Huang, Z., et al. (2019). RORgamma is a targetable master regulator of cholesterol biosynthesis in a cancer subtype. Nat. Commun. *10*, 4621. https://doi.org/10.1038/s41467-019-12529-3.
31. Cafforio, P., Dammacco, F., Gernone, A., and Silvestris, F. (2005). Statins activate the mitochondrial pathway of apoptosis in human lymphoblasts and myeloma cells. Carcinogenesis *26*, 883–891. https://doi.org/10.1093/carcin/bgi036.
32. Klein, A.M., Biderman, L., Tong, D., Alaghebandan, B., Plumber, S.A., Mueller, H.S., van Vlimmeren, A., Katz, C., and Prives, C. (2021). MDM2, MDMX, and p73 regulate cell-cycle progression in the absence of wild-type p53. Proc. Natl. Acad. Sci. USA *118*, e2102420118. https://doi.org/10.1073/pnas.2102420118.
33. Mendrysa, S.M., McElwee, M.K., Michalowski, J., O'Leary, K.A., Young, K.M., and Perry, M.E. (2003). mdm2 Is critical for inhibition of p53 during lymphopoiesis and the response to ionizing irradiation. Mol. Cell Biol. *23*, 462–472.
34. Maetens, M., Doumont, G., Clercq, S.D., Francoz, S., Froment, P., Bellefroid, E., Klingmuller, U., Lozano, G., and Marine, J.C. (2007). Distinct roles of Mdm2 and Mdm4 in red cell production. Blood *109*, 2630–2633. https://doi.org/10.1182/blood-2006-03-013656.
35. Zhang, Z., Wang, H., Li, M., Agrawal, S., Chen, X., and Zhang, R. (2004). MDM2 is a negative regulator of p21WAF1/CIP1, independent of p53. J. Biol. Chem. *279*, 16000–16006. https://doi.org/10.1074/jbc.M312264200.
36. Manfredi, J.J. (2010). The Mdm2-p53 relationship evolves: Mdm2 swings both ways as an oncogene and a tumor suppressor. Genes Dev. *24*, 1580–1589. https://doi.org/10.1101/gad.1941710.
37. Secchiero, P., Zerbinati, C., Melloni, E., Milani, D., Campioni, D., Fadda, R., Tiribelli, M., and Zauli, G. (2007). The MDM-2 antagonist nutlin-3 promotes the maturation of acute myeloid leukemic blasts. Neoplasia *9*, 853–861. https://doi.org/10.1593/neo.07523.
38. Falk, I.J., Willander, K., Chaireti, R., Lund, J., Nahi, H., Hermanson, M., Gréen, H., Lotfi, K., and Söderkvist, P. (2015). TP53 mutations and MDM2(SNP309) identify subgroups of AML patients with impaired outcome. Eur. J. Haematol. *94*, 355–362. https://doi.org/10.1111/ejh.12438.
39. Adelman, E.R., Huang, H.T., Roisman, A., Olsson, A., Colaprico, A., Qin, T., Lindsley, R.C., Bejar, R., Salomonis, N., Grimes, H.L., and Figueroa, M.E. (2019). Aging Human Hematopoietic Stem Cells Manifest Profound Epigenetic Reprogramming of Enhancers That May Predispose to Leukemia. Cancer Discov. *9*, 1080–1101. https://doi.org/10.1158/2159-8290.CD-18-1474.
40. Jaiswal, S., and Ebert, B.L. (2019). Clonal hematopoiesis in human aging and disease. Science *366*, eaan4673. https://doi.org/10.1126/science.aan4673.
41. Pang, W.W., Price, E.A., Sahoo, D., Beerman, I., Maloney, W.J., Rossi, D.J., Schrier, S.L., and Weissman, I.L. (2011). Human bone marrow hematopoietic stem cells are increased in frequency and myeloid-biased with age. Proc. Natl. Acad. Sci. USA *108*, 20012–20017. https://doi.org/10.1073/pnas.1116110108.
42. Mejia-Ramirez, E., and Florian, M.C. (2020). Understanding intrinsic hematopoietic stem cell aging. Haematologica *105*, 22–37. https://doi.org/10.3324/haematol.2018.211342.
43. Konopleva, M., Martinelli, G., Daver, N., Papayannidis, C., Wei, A., Higgins, B., Ott, M., Mascarenhas, J., and Andreeff, M. (2020). MDM2 inhibition: an important step forward in cancer therapy. Leukemia *34*, 2858–2874. https://doi.org/10.1038/s41375-020-0949-z.
44. Kojima, K., Konopleva, M., Samudio, I.J., Shikami, M., Cabreira-Hansen, M., McQueen, T., Ruvolo, V., Tsao, T., Zeng, Z., Vassilev, L.T., and Andreeff, M. (2005). MDM2 antagonists induce p53-dependent apoptosis in AML: implications for leukemia therapy. Blood *106*, 3150–3159. https://doi.org/10.1182/blood-2005-02-0553.
45. Prives, C., and White, E. (2008). Does control of mutant p53 by Mdm2 complicate cancer therapy? Genes Dev. *22*, 1259–1264. https://doi.org/10.1101/gad.1680508.
46. Terzian, T., Suh, Y.A., Iwakuma, T., Post, S.M., Neumann, M., Lang, G.A., Van Pelt, C.S., and Lozano, G. (2008). The inherent instability of mutant p53 is alleviated by Mdm2 or p16INK4a loss. Genes Dev. *22*, 1337–1344. https://doi.org/10.1101/gad.1662908.
47. Yan, B., Chen, Q., Xu, J., Li, W., Xu, B., and Qiu, Y. (2020). Low-frequency TP53 hotspot mutation contributes to chemoresistance through clonal expansion in acute myeloid leukemia. Leukemia *34*, 1816–1827. https://doi.org/10.1038/s41375-020-0710-7.
48. Kucab, J.E., Hollstein, M., Arlt, V.M., and Phillips, D.H. (2017). Nutlin-3a selects for cells harbouring TP53 mutations. Int. J. Cancer *140*, 877–887. https://doi.org/10.1002/ijc.30504.
49. Daver, N.G., Dail, M., Garcia, J.S., Jonas, B.A., Yee, K.W.L., Kelly, K.R., Vey, N., Assouline, S., Roboz, G.J., Paolini, S., et al. (2023). Venetoclax and idasanutlin in relapsed/refractory AML: a nonrandomized, open-label phase 1b trial. Blood *141*, 1265–1276. https://doi.org/10.1182/blood.2022016362.
50. Boettcher, S., Miller, P.G., Sharma, R., McConkey, M., Leventhal, M., Krivtsov, A.V., Giacomelli, A.O., Wong, W., Kim, J., Chao, S., et al.

(2019). A dominant-negative effect drives selection of TP53 missense mutations in myeloid malignancies. Science *365*, 599–604. https://doi.org/10.1126/science.aax3649.

51. Wang, Z., Burigotto, M., Ghetti, S., Vaillant, F., Tan, T., Capaldo, B.D., Palmieri, M., Hirokawa, Y., Tai, L., Simpson, D.S., et al. (2024). Loss-of-Function but Not Gain-of-Function Properties of Mutant TP53 Are Critical for the Proliferation, Survival, and Metastasis of a Broad Range of Cancer Cells. Cancer Discov. *14*, 362–379. https://doi.org/10.1158/2159-8290.CD-23-0402.
52. Alt, J.R., Greiner, T.C., Cleveland, J.L., and Eischen, C.M. (2003). Mdm2 haplo-insufficiency profoundly inhibits Myc-induced lymphomagenesis. EMBO J. *22*, 1442–1450. https://doi.org/10.1093/emboj/cdg133.
53. Eischen, C.M., and Boyd, K. (2012). Decreased Mdm2 expression inhibits tumor development and extends survival independent of Arf and dependent on p53. PLoS One *7*, e46148. https://doi.org/10.1371/journal.pone.0046148.
54. Boeva, V., Popova, T., Bleakley, K., Chiche, P., Cappo, J., Schleiermacher, G., Janoueix-Lerosey, I., Delattre, O., and Barillot, E. (2012). Control-FREEC: a tool for assessing copy number and allelic content using next-generation sequencing data. Bioinformatics *28*, 423–425. https://doi.org/10.1093/bioinformatics/btr670.
55. Wang, K., Li, M., and Hakonarson, H. (2010). ANNOVAR: functional annotation of genetic variants from high-throughput sequencing data. Nucleic Acids Res. *38*, e164. https://doi.org/10.1093/nar/gkq603.

STAR★METHODS

KEY RESOURCES TABLE

REAGENT or RESOURCE	SOURCE	IDENTIFIER
Chemicals, peptides, and recombinant proteins		
4% paraformaldehyde	Invitrogen	Cat# FB002
Optimal Cutting Temperature (OCT)	Tissue-Tek	Cat# 4583
5-Iodo-2′-deoxyuridine (IdU)	Acros Organics	Cat# AC122350000
MitoSOX Red	Molecular Probes	Cat# M36008
C11 BODIPY 581/591	Molecular Probes	Cat# D-3861
Methylcellulose-based medium (MethoCult)	StemCell Technologies	Cat# M3534 or M3434
RBC lysis buffer	BD Biosciences	Cat# 555899
Protease/Phosphatase Inhibitor Cocktail	Cell Signaling	Cat# 5872
Xylene	Fisher Scientific	Cat# X5-1
Ethanol, Absolute	Fisher Scientific	Cat# E7023
Hydrogen Peroxide, 3% Solution	Sigma-Aldrich	Cat# H1009
Hematoxylin	Sigma-Aldrich	Cat# MHS16
Antibodies		
Rabbit monoclonal anti-Ki67	Abcam	Cat# ab15580
Rabbit polyclonal anti-p53	Leica	Cat# CM5P-L
Rat monoclonal anti-CD3	Biolegend	Cat# 100202
Chicken anti-Goat IgG Alexa Fluor 647	Invitrogen	Cat# A-21469
Donkey anti-Rabbit IgG Alexa Fluor 647	Invitrogen	Cat# A-31573
DAPI	Life Technologies	Cat# D3571
VECTASHIELD Mounting Medium	Fisher	Cat# H-1000
CD117 (c-Kit) PE/Cy7	BioLegend	Cat# 105814
Ly-6A/E (Sca-1) Alexa Fluor 700	BD Biosciences	Cat# 565981-82
Lineage Cocktail Pacific Blue	BioLegend	Cat# 133306
CD150 APC (SLAM)	BioLegend	Cat# 115910
CD19 FITC	BD Biosciences	Cat# 557398
CD11 b PE	BD Biosciences	Cat# 557397
Ly6G APC Cy7	BD Biosciences	Cat# 560600
CD3 PE	BD Biosciences	Cat# 555275
SREBP2 antibody	Invitrogen	Cat# PA1-338
MDM2 antibody	Sigma-Aldrich	Cat# M4308
Sqle antibody	Cell Signaling	Cat# 40659
p21 antibody	Cell Signaling	Cat# 556430
eIF2a antibody	Cell Signaling	Cat# 2103
Phospho-eIF2a (Ser51) antibody	Cell Signaling	Cat# 53085
ATF-4 antibody	Cell Signaling	Cat# 11815
b-actin antibody	Cell Signaling	Cat# A5316
Alpha-tubulin antibody	Cell Signaling	Cat# 2125
Histone H3 antibody	Cell Signaling	Cat# 3638
Software and algorithms		
PhenoChart	PerkinElmer	Available from PerkinElmer
Vectra Polaris	PerkinElmer	PerkinElmer
Experimental models: Organisms/strains		
Mdm2-floxed mice	Jackson Laboratory	Mdm2tm2.1Glo/J

(*Continued on next page*)

Continued

REAGENT or RESOURCE	SOURCE	IDENTIFIER
mTmG mice	Jackson Laboratory	B6.129(Cg)-Gt(ROSA)26Sortm4 (ACTB-tdTomato,-EGFP)Luo/J
Ai14 reporter	Jackson Laboratory	RosaLsl-TdTomato
Trp53-floxed mice	Jackson Laboratory	B6.129P2-Trp53tm1Brn/J
Vav-Cre mice	Jackson Laboratory	B6.Cg-Commd10Tg(Vav1-icre)A2Kio/J
Mx1-cre mice	Jackson Laboratory	B6.Cg-Tg1Cgn/J
Trp53 wmR172H mice	Previously described	Pourebrahim et al.[19] and Zhang et al.[20]
Deposited data		
Differential gene expression data of murine LK cells in *Mdm2* haploinsufficient mice	This paper	Dryad: https://doi.org/10.5061/dryad.s4mw6m9dr

RESOURCE AVAILABILITY

Lead contact

Further information and requests for resources and reagents should be directed to and will be fulfilled by the lead contact, Michael Andreeff (mandreef@mdanderson.org).

Materials availability

All unique/stable reagents generated in this study are available from the lead contact with a completed Materials Transfer Agreement.

Data and code availability

- All primary microscopy and western blot data generated in this study are available from the lead contact upon request.
- This paper does not report original code.
- Any additional information required to reanalyze or reproduce data reported in this paper is available from the lead contact upon request.

EXPERIMENTAL MODEL AND STUDY PARTICIPANT DETAILS

Animal studies

The following mouse models were utilized in this study: *Mdm2*-floxed mice (*Mdm2*$^{tm2.1Glo/J}$), mTmG mice (B6.129(Cg)-*Gt(ROSA)26Sor*$^{tm4(ACTB-tdTomato,-EGFP)Luo}$/J), Ai14 reporter (*Rosa*$^{Lsl-TdTomato}$), *Trp53*-floxed mice (B6.129P2-*Trp53*^{tm1Brn}/J), *Vav-Cre* mice (B6.Cg-*Commd10*$^{Tg(Vav1-icre)A2Kio}$/J), and *Mx1-cre (B6.Cg-Tg1Cgn/J)*, which were obtained from the Jackson Laboratory. *Trp53* ^{wmR172H} mice were previously described.[19,20] Male and female mice aged between 2 and 6 months were used for the transplantation experiments, ensuring age-matching within each experimental group. Activation of the *Mx1-Cre* recombinase was achieved by intraperitoneal injections of pIpC. Genotyping was conducted by PCR analysis using tail DNA samples. All animals were housed in compliance with the approved protocols of the Institutional Animal Care and Use Committee (IACUC) at MD Anderson.

METHOD DETAILS

Fluorescence microscopy

Isolated tissues were fixed in 4% paraformaldehyde in phosphate-buffered saline (PBS) (Invitrogen, FB002) overnight. Bones were washed in PBS and decalcified in 14% EDTA solution for 10 days at 4°C. Bone samples were subsequently washed in PBS and immersed in 30% sucrose PBS solution overnight. Bones and soft tissues were transferred and submerged in optimal cutting temperature (OCT) compound (Tissue-Tek, 4583). The embedded tissue was cut into 5-μm sections using a cryostat. The sections were then stored as frozen slides at −80°C or further processed. For further processing, tissue slides were washed with PBS and then incubated in 3% BSA for 1 h at room temperature. After three subsequent 5-min washes in PBS, primary antibody incubation against anti-Ki67 antibody (Abcam, ab15580), p53 (CM5, Leica P53-CM5P-L), and CD3 (BioLegend, 100202) was performed at antibody-specific dilutions in a light-protected hydration chamber at 4°C. Secondary antibody staining against the primary antibody host species (Chicken anti-Goat IgG Alexa Fluor 647, Invitrogen, A-21469; and Donkey anti-Rabbit IgG Alexa Fluor 647, Invitrogen, A-31573) was done at dilutions of 1:500 for 1 h at room temperature. Tissue slides were washed thrice in PBS for 5 min, stained with DAPI (Life Technologies, D3571) at 1:750 for 5 min and rinsed with PBS. Slides were mounted with VECTASHIELD Mounting Medium (Fisher, H-1000) and sealed with nail polish.

CyTOF analysis

Bone marrow samples were collected using aseptic techniques by flushing the long bones with cold PBS. After removing red blood cells (RBC lysis), the bone marrow suspension was transferred to sterile tubes. To eliminate contaminants, the cell pellet was washed multiple times with PBS. A panel of 31 antibodies, targeting specific cellular markers of interest in the bone marrow, was designed and selected (Table S2). Antibody cocktails were prepared by combining the individual antibodies in appropriate dilution buffers. The bone marrow cells obtained from the pellet were resuspended in staining buffer, and the antibody cocktails were added to the cell suspension. The mixture was then incubated in the dark at room temperature to allow the antibodies to bind to the target markers. Next, the stained cell suspension was loaded onto the CyTOF instrument. To mark cells in the S-phase of the cell cycle, the cells were labeled with 5-Iodo-2′-deoxyuridine (IdU) (Acros Organics) at a final concentration of 10 μM IdU for 30 min at 37°C. Following intracellular staining, the cells were washed twice and resuspended in an intercalator solution (1.6% paraformaldehyde in PBS with 125 nM iridium nucleic acid intercalator). The suspension was then incubated at 4°C overnight and acquired at a rate of 300 events per second on the Helios instrument, using CyTOF Software version 6.7.1016 (Standard Bio Tools, San Francisco, CA). Subsequently, data processing of samples was performed using FlowJo version 10.8.1.

Imaging and spectral unmixing

Frozen tissue sections and immunofluorescence-stained slides were imaged using a Vectra Multispectral Imaging System version 2 (Akoya Biosciences) at a magnification of 40×. The images were then visualized using Phenochart slide viewer software (Akoya Biosciences). Spectral unmixing was performed using inForm Analysis software (Akoya Biosciences), as previously described. Briefly, the software identifies the spectral signature of each fluorescent probe in the sample and separates overlapping signals into distinct channels based on their unique spectral properties. This process allows for accurate identification and quantification of individual markers in complex samples.

Flow cytometry and ROS analysis

Bone marrow (BM) single-cell suspensions were obtained by intrafemoral flushing and crushing of bone, followed by filtration through 40-μm strainers (Fisher, 08-771-1). Red blood cells (RBCs) were lysed in 1x RBC lysis buffer (BD Biosciences, 555899) for 15 min with slight agitation at room temperature. After two washes in PBS, cells were stained with the following antibodies: CD117 (c-Kit) PE/Cy7 (Biolegend, 105814), Ly-6A/E (Sca-1) Alexa Fluor 700 (BD Bioscience, 565981-82), Lineage Cocktail Pacific Blue (BioLegend, 133306), CD150 APC (SLAM) (BioLegend, 115910), CD19 FITC (BD Biosciences, 557398), CD11 b PE (BD Biosciences, 557397), Ly6G APC Cy7 (BD Biosciences, 560600), and CD3 PE (BD Biosciences, 555275).

To assess oxidative stress upon irradiation, cells were stained with MitoSOX Red (Molecular Probes, M36008) or C11 BODIPY 581/591 (Molecular Probes, D-3861), together with Ghost Dye Violet 540 (Tonbo Biosciences, 13–0879) and the aforementioned surface marker antibodies. Mitochondrial oxidative stress was determined by the percentage of cells exhibiting a high MitoSOX signal, while lipid peroxidation was assessed by the fluorescence ratio of oxidized signal (510 nm) to reduced signal (590 nm) on flow cytometry. The gating strategy is described in the Figure S8. Data were collected and analyzed using the Beckman Coulter Gallios Flow Cytometer and Kaluza Analysis Software.

Colony assays

Isolated total bone marrow and/or progenitor cells from mice were plated at a concentration of 50,000 cells in 2 mL of methylcellulose methylcellulose-based medium (MethoCult M3534 or M3434; StemCell Technologies, Canada), containing IL-3, IL-6, mSCF, EPO. After 5–7 days, colonies were scored microscopically, harvested, and replated up to 5 times. For liquid culture assays, we washed 30,000 cells in PBS and resuspended them in either RPMI 1640 with FBS, Pen/Strep, and various growth factors, or Xvivo Medium supplemented with Flt3-ligand, mSCF, TPO.

Immunoblot analysis

Mouse BM cells were collected, and RBCs were lysed in 1x RBC lysis buffer. After *ex vivo* irradiation of 400 cGy, cells were lysed at a density of 1×10^6/50 μL in protein lysis buffer (0.25 M Tris-HCl, 2% SDS, 4% β-mercaptoethanol, 10% glycerol, 0.02% bromophenol blue) supplemented with Protease/Phosphatase Inhibitor Cocktail (Cell Signaling) and incubated at 95°C for 5 min for denaturing. Immunoblot analysis was performed as previously reported with some modifications. Briefly, an equal amount of protein lysate was resolved using 4–12% Bir-Tris Mini Protein Gels (Invitrogen) and transferred to polyvinylidene fluoride (PVDF) membranes. Membranes were divided, probed for target proteins, and imaged (Odyssey imaging system, LI-COR). Primary antibodies used were as follows: SREBP2 (Invitrogen, PA1-338), MDM2 (Sigma-Aldrich, M4308), Sqle (Cell Signaling #40659), p21 (BD #556430), eIF2α (cell signaling #2103), Phospho-eIF2α (Ser51) (cell signaling #53085), ATF-4 (cell signaling #11815), β-actin (Sigma-Aldrich A5316), p53 (Leica, NCL-L-p53-CM5p), alpha-tubulin (Cell Signaling #2125), and histone H3 (Cell Signaling #3638). IRDye 680LT Donkey anti-Mouse IgG and 800CW Donkey anti-Rabbit IgG (LI-COR Biosciences) were used as secondary antibodies.

Evaluation of cytotoxicity and synergism in AML cell lines

AML cell lines (MOLM13, OCIAML2 and OCIAML3) were seeded at a density of 15,000 cells per well in 96 well plate containing complete RPMI-1640 medium supplemented with 10% fetal calf serum. The cells were treated for 48 h with Atorvastatin at doses ranging

from 0 to 10 μM and Nutlin (N3a) at doses ranging from 0 to 5 μM, resulting in a 6 × 6 matrix of treatment. Each experiment was conducted independently three times. Viable cell numbers were assessed by quantifying ATP using the CellTiter-Glo Luminescent Cell Viability Assay (Promega). The results were normalized to the values obtained for DMSO-treated cells and expressed as a percentage of control. Dose-response curves were analyzed using a curve-fitting routine based on nonlinear regression to calculate the EC50 value. Additionally, synergistic effects of Atorvastatin with Nutlin were determined based on the mean values obtained from three independent experiments. Synergy evaluation was performed by collecting, processing, and visualizing the data using the BLISS Index method with COMBENEFIT software.

Immunohistochemical analysis

Immunohistochemical analysis was performed to investigate the expression of p53 protein in formalin-fixed paraffin-embedded tissue sections. The VECTASTAIN Elite ABC HRP Kit (Vector Laboratories, Pk-6101) was used for the immunohistochemical staining. Formalin-fixed paraffin-embedded tissue sections were deparaffinized by immersion in two changes of xylene, followed by two changes of 100% ethanol. Subsequently, the sections were passed through 95%, 75%, and 50% ethanol for 5 min per change. To block endogenous peroxidase activity, the tissue sections were immersed in a 3% H2O2 solution in methanol for 10 min. The antigen retrieval process was performed by immersing the slides in Coplin jars containing antigen retrieval solution. The slides were then placed in an IHC-Tek Epitope Retrieval Steamer (IHC World, IW-1102) and steamed for 10 min. Afterward, the slides were allowed to cool down for 20 min at room temperature. To prevent non-specific binding, the slides were blocked for 60 min with 10% serum in 0.1% TBST (Tris-buffered saline with Tween 20). The primary antibody against p53 (CM5, Leica P53-CM5P-L) was diluted in 2% FBS (fetal bovine serum) in 0.1% TBST and incubated overnight at 4°C in a light-protected hydration chamber. Following the primary antibody incubation, the slides were washed twice for 5 min each in Tris-buffered saline (TBS). The slides were incubated with the biotinylated secondary antibody solution for 30 min at room temperature. Slides were washed twice for 5 min each in TBS. Slides were incubated with ABC solution for 30 min and washed twice for 5 min each in phosphate-buffered saline (PBS). The slides were incubated in the 3,3′-Diaminobenzidine (DAB) solution until the desired signal intensity was achieved. Excess DAB solution was washed off with deionized water, and the slides were counterstained with hematoxylin for 80 s. Slides were immersed in lithium carbonate solution for 60 s, followed by immersion in deionized water for 10 min. The slides were sequentially immersed in 95% ethanol and 100% ethanol for 90 s per change (two changes for each). Slides were immersed three times for 5 min each in xylene. Finally, the slides were mounted with Richard-Allan Scientific Mounting Medium (Thermo Scientific, 4112) for preservation and analysis. The immunohistochemically stained slides were then examined under a microscope to assess the expression pattern and intensity of p53 protein in the tissue samples.

Cell blood counts

Mouse peripheral blood (50 μL) was collected into BD Microtainer vials (Fisher, 02-669-33) via retro-orbital bleeding. Blood samples were analyzed on the Horiba ABX SAS PENTRA 60 C+ cell blood counter to identify hematopoietic irregularities.

RNA sequencing

RNA was extracted utilizing the Direct-Zol RNA Microprep kit (Zymo Research, R2060). Barcoded Illumina-compatible stranded total RNA libraries were prepared using the TruSeq Stranded Total RNA kit (Illumina) as previously described.[19] Library pools were quantified by qPCR and sequenced on the HiSeq 4000 sequencer using the 75-bp paired-end format. The raw RNA-seq readouts were subsequently mapped to the mouse mm10 assembly reference genome using TopHat2 and analyzed with DESeq2 (Bioconductor package).

Whole exome sequencing

Dual-indexed libraries compatible with Illumina were created using 15ng–50ng of genomic DNA, which had been sheared by a Biorupter Ultrasonicator (Diagenode) and treated with RNase. This DNA was processed using the Twist Library Preparation Kit and the Twist Universal Adapter System, following the manufacturer's instructions. The libraries, indexed and prepared for capture, underwent 6 cycles of PCR amplification with Twist UDI primers. Their fragment size distribution was then evaluated using the 4200 TapeStation High Sensitivity D1000 ScreenTape (Agilent Technologies), and their concentration was determined with the Qubit dsDNA HS Assay Kit (ThermoFisher). After normalizing the concentrations, equal amounts of the uniquely dual-indexed libraries were pooled together, with 7 libraries in each pool. For exon targeting, the Twist Mouse Core Exome kit was employed. Post-capture, the enriched exon library pools were further amplified with 6 PCR cycles. Size distribution was again assessed with the 4200 TapeStation High Sensitivity D1000 ScreenTape (Agilent Technologies), and concentration measurements were taken using the Qubit dsDNA HS Assay Kit. Quantification of the exon-enriched library pools was performed by qPCR utilizing the KAPA Library Quantification Kit (KAPABiosystems). Finally, these libraries were sequenced on a NovaSeq6000 SP-200 flow cell in a 100 nt PE format.

Copy number analysis

Copy number detection was conducted using the latest version of Control-FREEC.[54] This process involves using aligned reads (bam files) as input, from which Control-FREEC creates copy number and B-allele frequency profiles, incorporating tumor purity estimates and corrections. These profiles undergo normalization, segmentation, and analysis to assign copy number events to specific

genomic regions. With the inclusion of a matched normal sample, Control-FREEC is able to distinguish between somatic and germline events. A threshold representing 50% of a chromosome arm's length serves as the criterion for differentiating between broad and focal events. To mitigate false positives from hyper-segmentation, segments underwent filtering with an amplitude threshold set at a copy-difference of 0.35 on a log scale. The frequency of broad copy number changes was quantified, followed by an analysis of focal copy number changes using the GISTIC methodology, which identifies significant peaks of amplifications and deletions. The identified copy number events were classified into two categories based on their observed frequency: focal events, which are significantly smaller than a chromosome arm, and broad events, encompassing a chromosome arm or an entire chromosome.

MDM2^{SNP309} exploration

We used alleleCount (https://github.com/cancerit/alleleCount) on PCAWG tumor/germline BAM files at the *MDM2*^{SNP309} position (chr12:69,202,580 in hg19 coordinates) to compute variant allele frequency (VAF) (minimum count ≥ 5). In germlines, genotypes were directly assessed using VAF (T/T: VAF = 0; T/G: $0.35 \leq$ VAF ≤ 0.65; G/G: VAF = 1). Copy number profiles and whole-genome doubling (WGD) information were retrieved from consensus copy number data; https://dcc.icgc.org/releases/PCAWG/consensus_cnv). In tumors, the retained allele (either T or G) was assessed in cases with *MDM2* allelic imbalance where VAF was compared to copy number states of major and minor alleles, corrected for tumor purity. *MDM2* copy-number statuses (normal, gain, loss, and copy-neutral) were defined by considering baseline ploidy (adjusted for WGD). *TP53* mutation status was obtained from the PCAWG Drivers and Functional Interpretation Group. *TP53* single nucleotide variations and insertion/deletions were functionally annotated (e.g., missense, nonsense, frameshift) using ANNOVAR.[55]

DNA isolation and SNP genotyping

Genomic DNA was extracted from the BM samples isolated from AML patients at diagnosis using QIAamp DNA Blood Midi kit (Qiagen). Genotyping of SNP rs2279744 (*Mdm2*^{SNP309}) in intron 1 of the *MDM2* gene was performed with 50 ng of genomic DNA using TaqMan SNP Genotyping Assay, (human-SNP ID:rs2279744) and TaqMan Genotyping Mastermix (ThermoFisher). PCR reactions were carried out on a Quantstudio 6 Flex instrument and analyzed using TaqMan Genotyper Software (Applied Biosystems Life Technologies).

QUANTIFICATION AND STATISTICAL ANALYSIS

Means and standard deviations were calculated using GraphPad Prism 6 software. The Student's t test was used for comparative analysis between two groups. Analysis of variance was used to compare multiple groups. $p < 0.05$ was set as statistically significant. A p value of less than 0.05 was considered statistically significant. In figure legends, symbols *, **, ***, and **** denote p values of less than 0.05, 0.01, 0.001, and 0.0001, respectively, unless stated otherwise. All experimental procedures were replicated three times, and error bars in the figures denote mean ± standard deviation (SD) values, unless mentioned otherwise.

Cell Reports Medicine, Volume *5*

Supplemental information

Age-specific induction of mutant p53 drives clonal hematopoiesis and acute myeloid leukemia in adult mice

Rasoul Pourebrahim, Rafael Heinz Montoya, Hiroki Akiyama, Lauren Ostermann, Shayuan Khazaei, Muharrem Muftuoglu, Natalia Baran, Ran Zhao, Tom Lesluyes, Bin Liu, Joseph D. Khoury, Mihai Gagea, Peter Van Loo, and Michael Andreeff

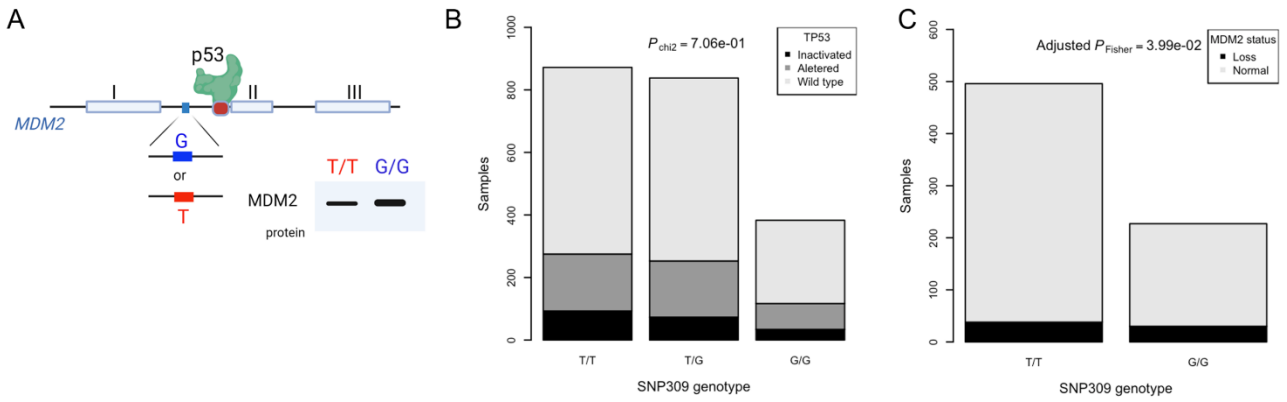

Supplementary Figure S1: *MDM2*^{SNP309} genotype is associated with *TP53* functional status, related to Figure 1. **A**) Schematic representation of *MDM2*^{SNP309} genomic locus and its association with MDM2 levels. The *MDM2*^{SNP309}G allele in the *MDM2* promoter near p53 binding site was shown to increase the levels of *MDM2* RNA and protein. **B**) Barplot of germline *MDM2* SNP309 genotype (T/T, T/G and G/G) depending on somatic *TP53* mutational status (inactivated, altered and wild type). There is no statistical difference amongst those categories (P_{chi2}=0.71). **C**) Barplot of germline *MDM2* ^{SNP309} genotype (T/T versus G/G) depending on *MDM2* copy-number status (loss and normal). This shows a significant difference in G/G cases where *MDM2* losses are more frequent than the ones in T/T cases (adjusted P_{Fisher}=3.99e-2).

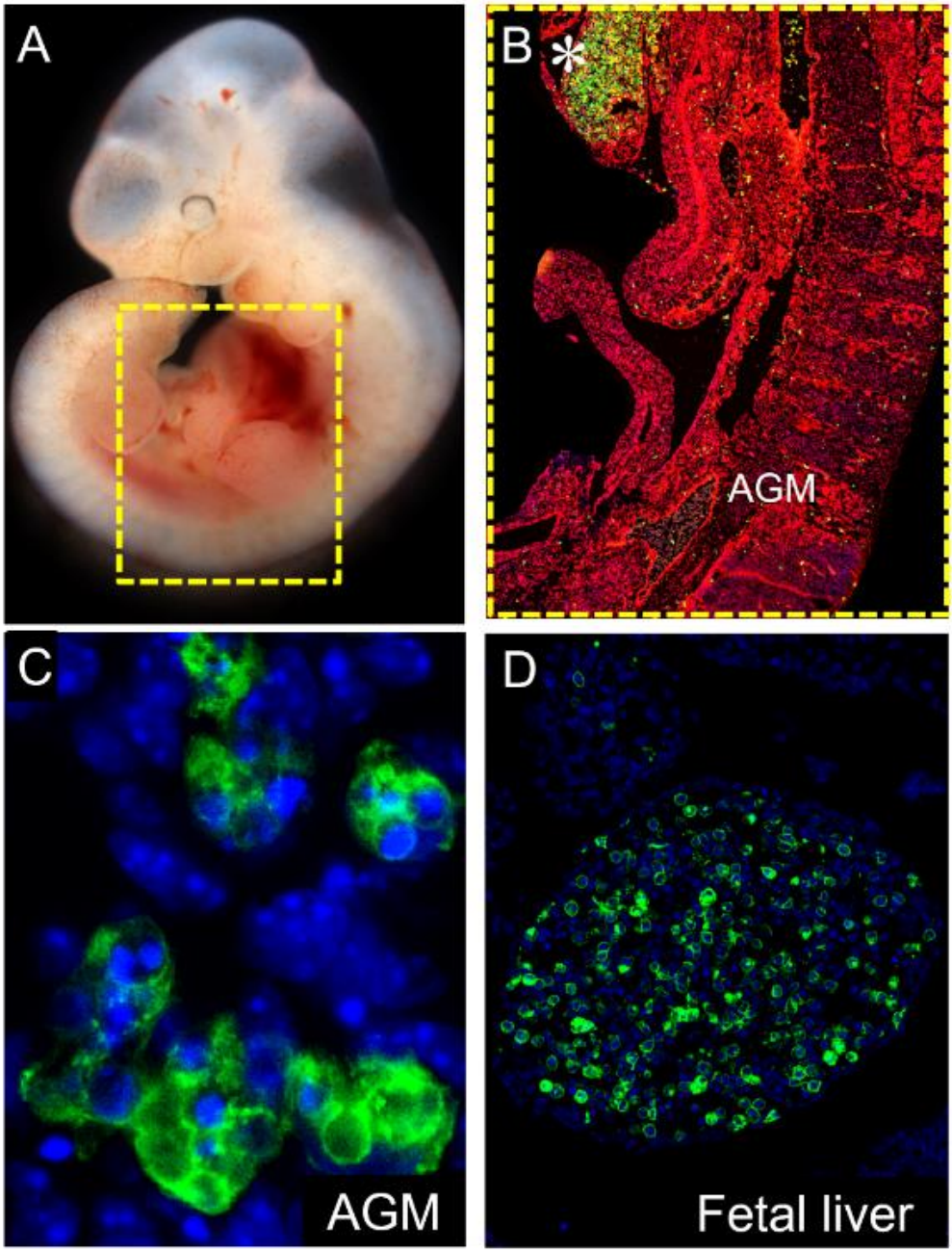

Supplementary Figure S2: *Vav-cre;mTmG* marks early HSCs in the AGM region, related to Figure 2. **A**) Microscopic view of a *Vav-cre;mTmG* mouse embryo at E10.5. The yellow dashed line indicates the AGM region. **B**) Direct fluorescence image of the region marked in panel A, showing the expression of membranous tomato (mT) throughout the whole embryo and membranous GFP (mG) in emerging hematopoietic cells in the AGM and fetal liver (asterisks). **C**) High magnification image of GFP-positive cells in the AGM. **D**) Representative image of GFP-positive cells in the fetal liver.

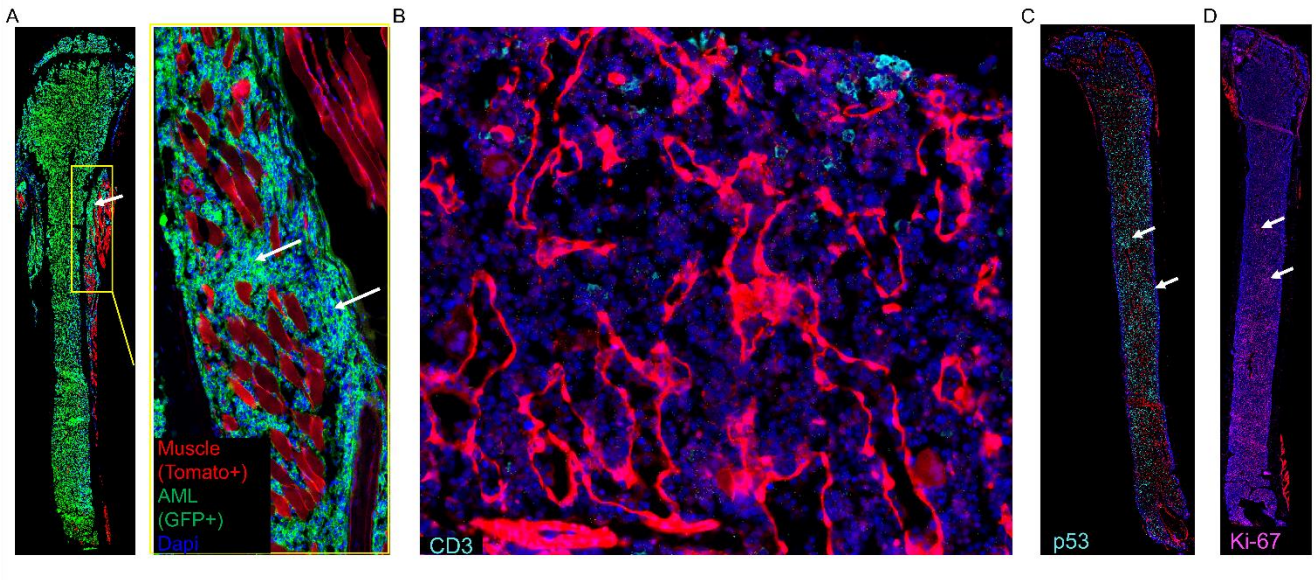

Supplementary Figure S3: Combination of *Mdm2* haploinsufficiency and mutant p53 results in highly proliferative AML, related to Figure 2. **A**) Direct fluorescence image of a longitudinal section of femur isolated from *Vav-Cre;Mdm2*$^{+/fl}$*; Trp53*$^{fl/wmR172H}$*;mTmG* mice with AML, illustrating a hypercellular bone marrow (GFP+) and non-hematopoietic cells (Tomato+). Leukemic cells are observed disrupting the periosteum and invading the muscle compartment (white arrows). **B**) Immunofluorescence image depicting the distribution of CD3+ cells (cyan) within the BM of an AML mouse, showing scattered CD3+ cells with few observed clusters. **C**) Immunofluorescence image illustrating the distribution of p53 mutant-expressing cells (cyan) in a bone marrow section obtained from the mouse mentioned in (A). The red color indicates stromal cells (Tomato+). **D**) Ki-67 expression (magenta) in a parallel section to C, demonstrating the distribution of proliferating cells (Ki-67+) throughout the BM.

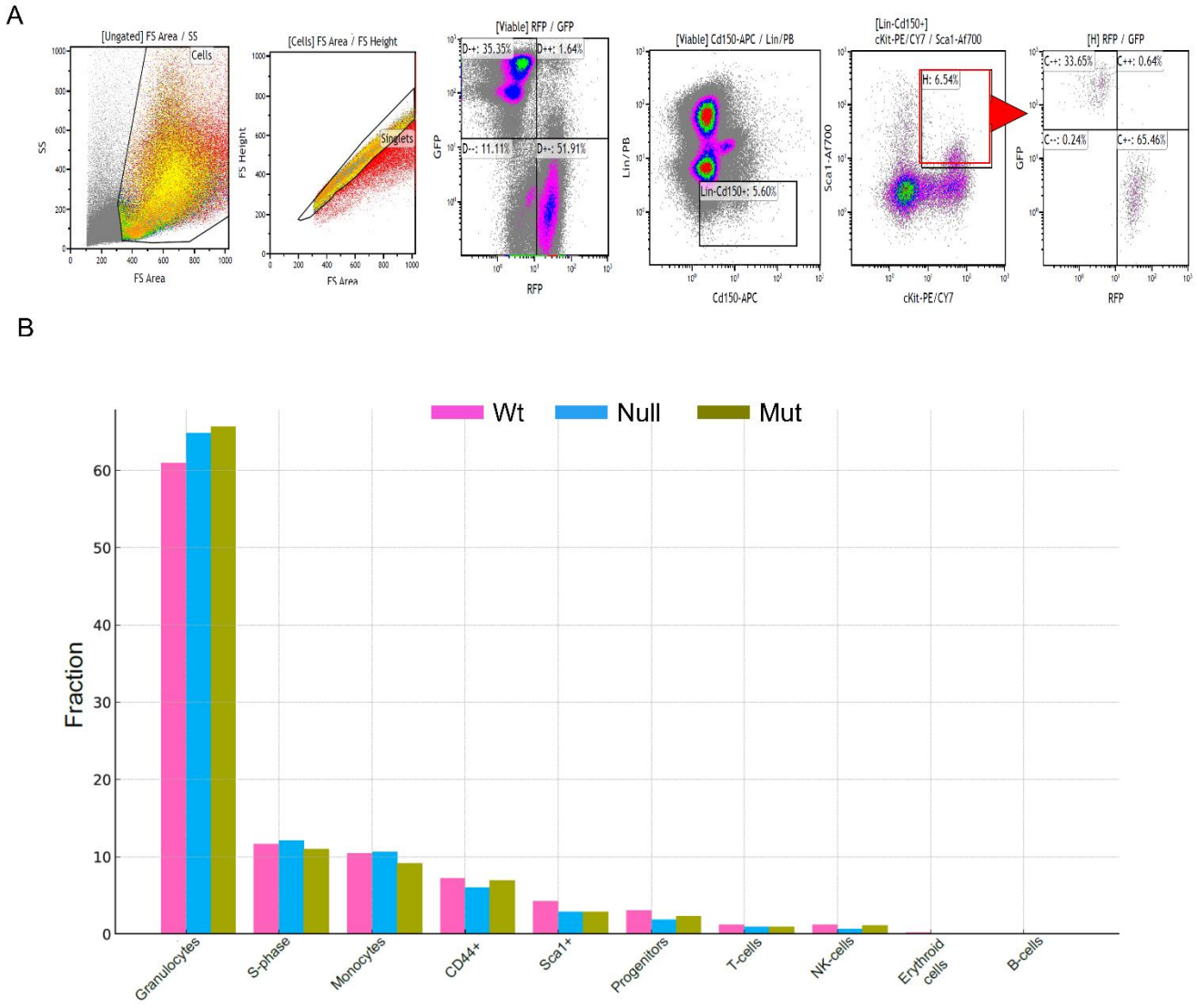

Supplementary Figure S4: Analysis of HSCs targeting and lineage characterization in *Mx1-Cre* mediated recombination and CyTOF profiling, related to Figure 3. **A**) *Mx1-Cre* effectively targets HSCs. A single-cell gate was created based on FSC and SSC parameters to exclude doublets and cell aggregates. To distinguish live cells from dead cells, a live/dead gating step was incorporated. The recombination of *mTmG* allele was confirmed by distinct population of GFP+ and RFP+. The LSK population was identified using a specific gate. LSK cells are characterized by being negative for lineage markers (Lin-) and positive for CD150, Sca-1 and c-Kit markers. After selecting the LSK population, the population of GFP and RFP cells were identified. **B**) Comprehensive characterization of cell lineages using CyTOF analysis in pooled BM samples isolated from *Mx1-Cre;mTmG (*p53 wild-type) ,*Mx1-Cre;Trp53*$^{fl/fl}$*;mTmG (*p53 null), and *Mx1-Cre;Trp53*$^{wmR172H/fl}$*;mTmG (*p53 mutant) mice. The bar plots summarize the subset frequencies in indicated genotypes.

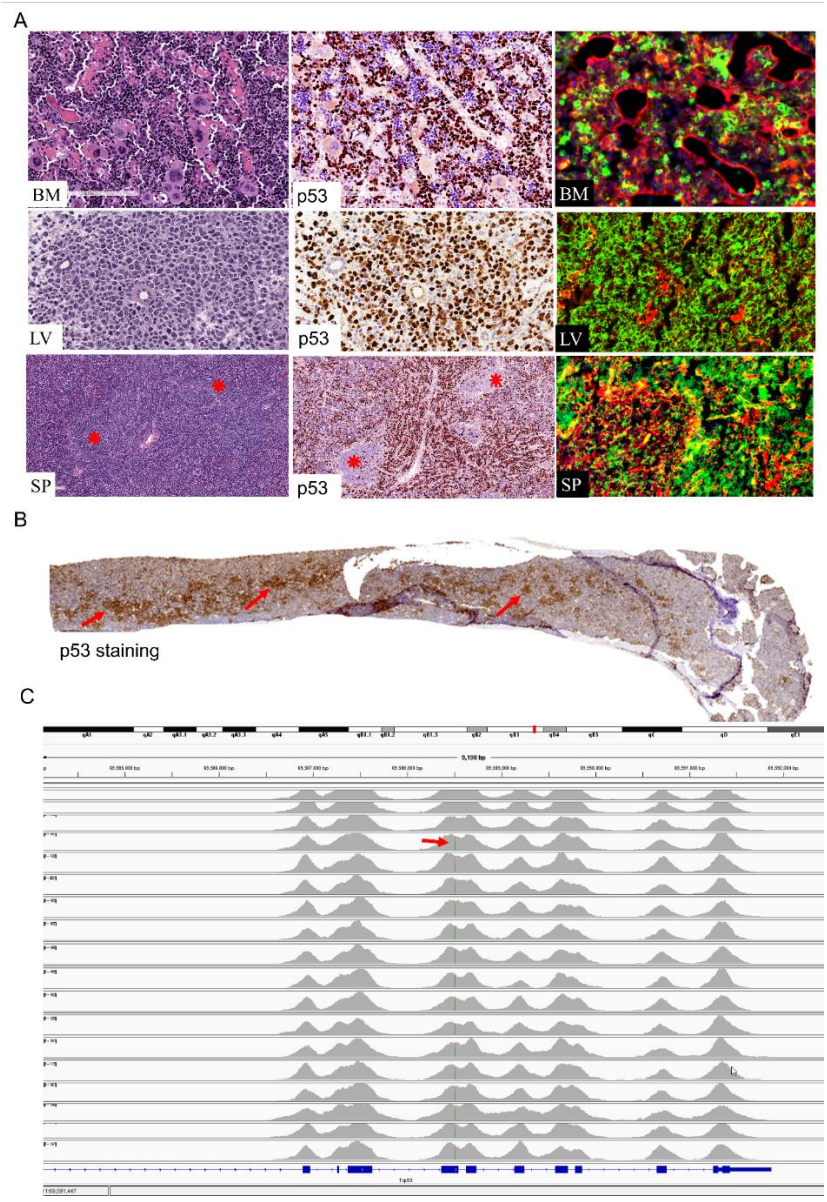

Supplementary Figure S5: Characterization of AML progression and genomic locus *in Mx1-Cre;Trp53*$^{wmR172H/fl}$*;mTmG* mice, related to Figure 4**.** **A**) Histological analysis of bone marrow (BM), liver (LV), and spleen (SP) tissues using hematoxylin and eosin (H&E) staining, revealing infiltration of leukemia cells. Notably, extensive infiltration of leukemia cells is observed in the spleen section, particularly in the periphery of the germinal center (red asterisks). Immunostaining of p53 protein in leukemia cells within BM, SP, and LV tissues is shown (brown staining). Furthermore, direct fluorescence visualization of BM, SP, and LV tissues demonstrates the presence of GFP+ leukemia cells. **B**) Immunostaining of p53 in a longitudinal section of the femur shows the clonal expansion of p53 mutant AML cells (red arrow). **C**) A snapshot of the IGV browser displaying the *Trp53* mutation in AML samples (red arrow).

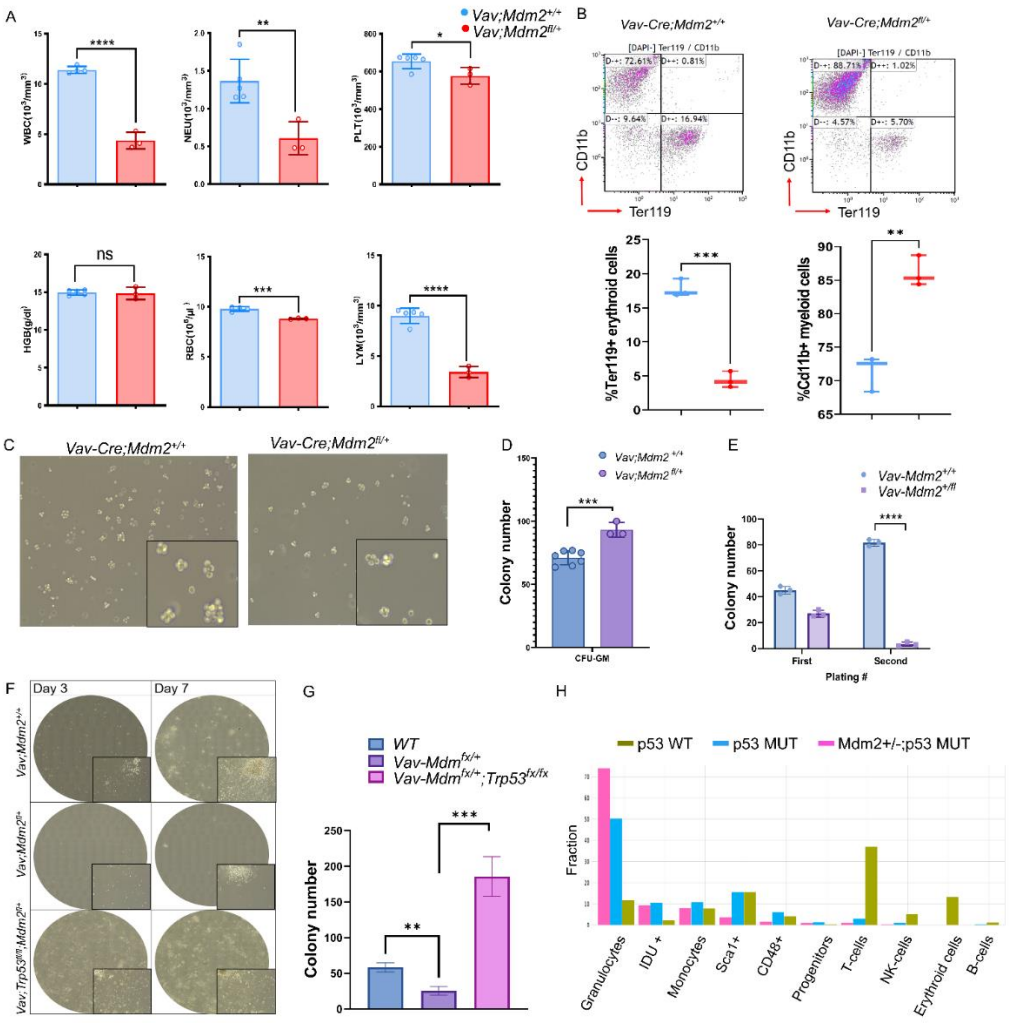

Supplementary Figure S6: Characterization of the hematopoietic phenotype of *Vav-cre;Mdm2*$^{fl/+}$ mice before and after deletion of p53, related to Figure 5. **A**) Peripheral blood indexes in *Vav-cre;Mdm2*$^{fl/+}$. Each plot represents the indicated blood cell type and shows the count values compared to control. Red Blood Cells (RBC), WBC (White Blood Cells), NEU (Neutrophils), LYM (Lymphocytes), PLT (Platelets), HGB (Hemoglobin). ****P < 0.0001, ***P < 0.001, **P < 0.01, *P < 0.5. **B**) Representative flow cytometry plots and quantification of CD11b+ myeloid cells and Ter119+ erythroid cells in CFU cells isolated from the indicated mice. **C**) Representative images of colonies from Vav-cre;Mdm2fl/+ and control mice. The high magnification view is shown in the black box. **D**) Quantification of granulocyte/macrophage colonies (means ± SDs). Each data point represents a measurement from an individual mouse. **E**) Colony number in methylcellulose replating assays using LSK cells from indicated mice. Mean ± SD. Statistical significance indicated by asterisks: ****P < 0.0001, n=3. **F**) Representative images of colonies in indicated mice at indicated time points. **G**) Quantification of colony numbers in (F). ***P < 0.001, **P < 0.01, n=3.

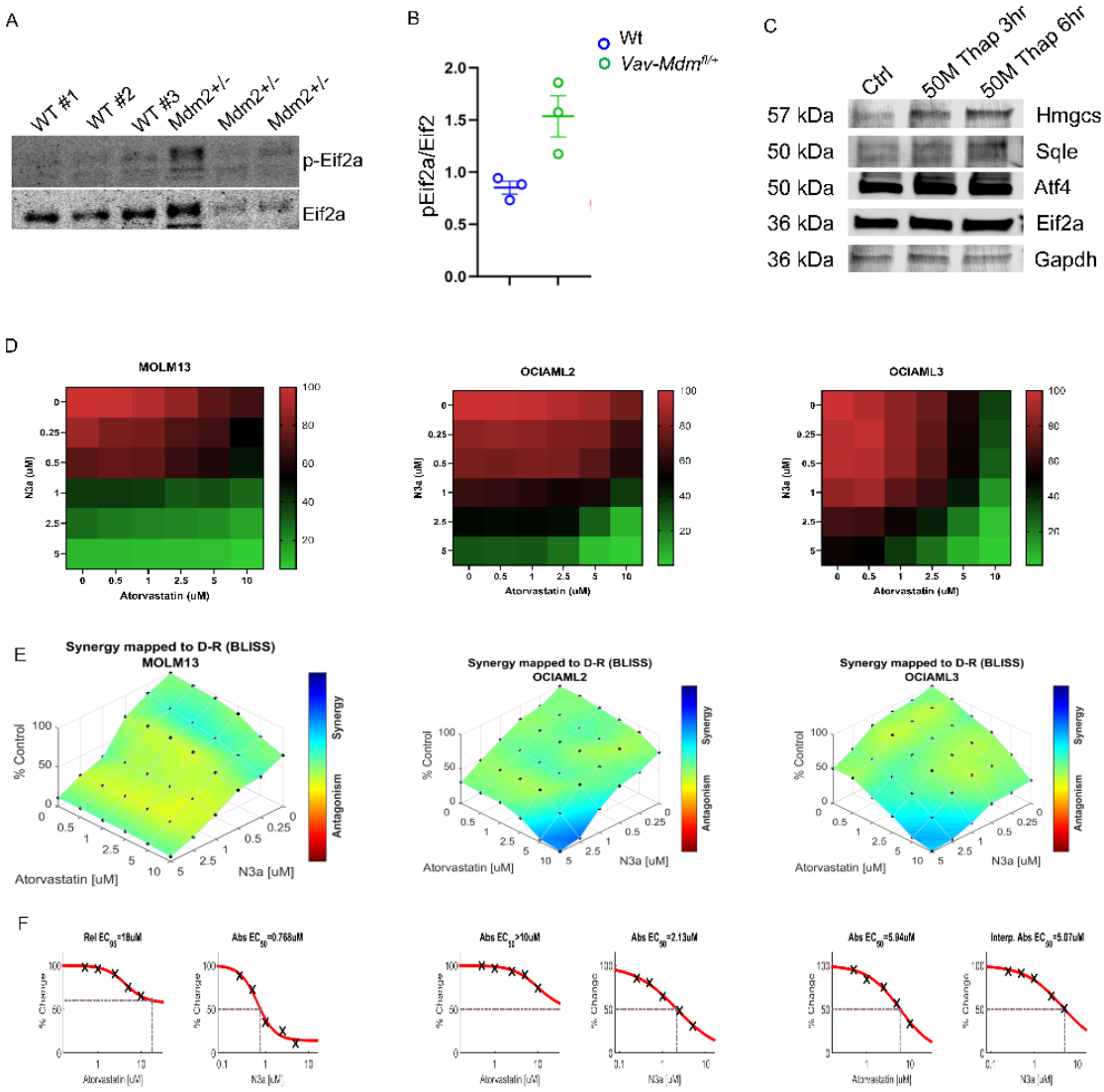

Supplementary Figure S7: ISR activation and therapeutic response assessment, related to Figure 6. **A**) Western blot analysis of phosphorylated eIF2α (p-Eif2a) and total Eif2a levels in BM cells derived from *Vav-Cre;Mdm2*$^{+/+}$ and *Vav-Cre;Mdm2*$^{+/fl}$ mice. **B**) Quantification of protein levels in (A). **C**) Western blot analysis of indicated proteins in K562 cells treated with the ISR activator, Thapsigargin, displaying bands corresponding to the molecular weights of the respective proteins. **D**) Matrix of cell viability under treatment with indicated doses of Atorvastatin (0-10 μM) and Nutlin (0-5 μM) in AML cell lines MOLM13, OCIAML3, and OCIAML2. Each square of the concentration matrix represents a mean value of independent experiments, normalized to levels in DMSO-treated controls, from 3 independent experiments, as measured by CTG assay. **E**) Results of delta BLISS index calculations for AML cell lines using COMBENEFIT software provided by Cancer Research UK Cambridge Institute. **F**) Dose response to single agents and EC50 estimation upon treatment with monotherapy: Atorvastatin and Nutlin. Each data point is expressed as the mean value, with n=3 independent experiments per condition.

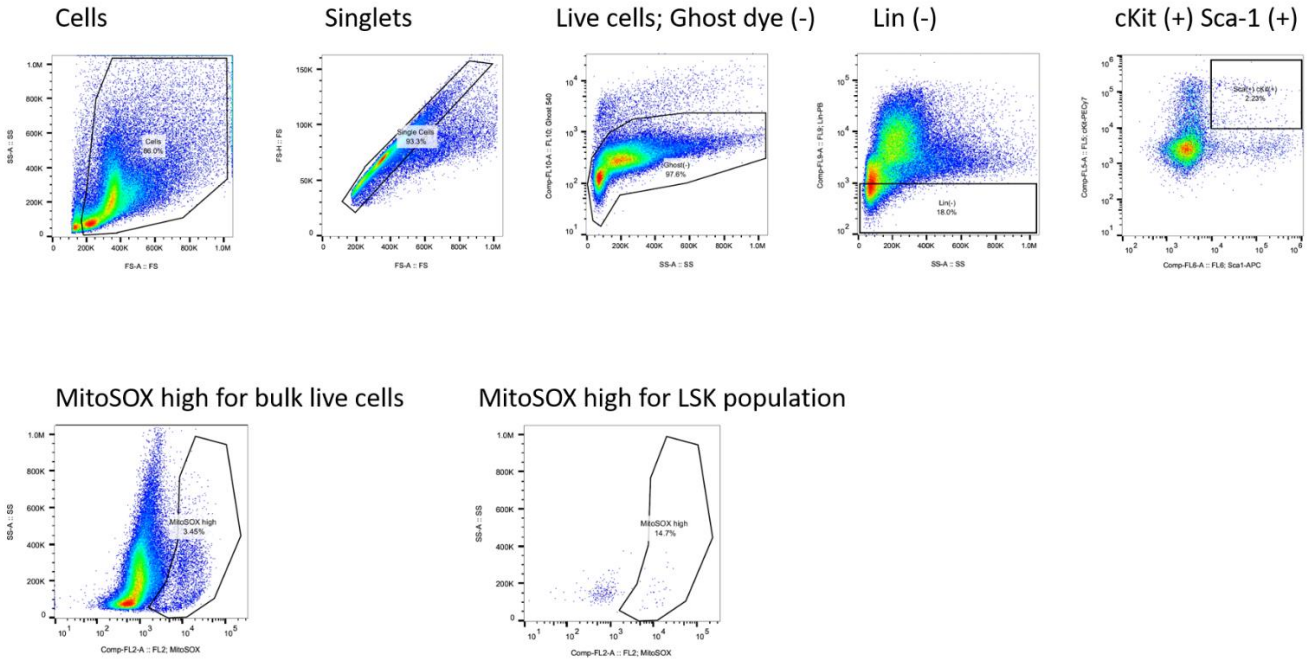

Supplementary Figure S8: Gating strategy for analysis of Mitosox in LSK cells, related to Figure 5. Before proceeding with Mitosox analysis, we applyed appropriate compensation to correct for spectral overlap between fluorochromes used in the experiment. Additionally, appropriate forward scatter (FSC) and side scatter (SSC) parameters were established to exclude debris and other non-cellular events. A single-cell gate was created based on FSC and SSC parameters to exclude doublets and cell aggregates. A live/dead gating step was incorporated to distinguish live cells from dead cells. Next, a gate was applied to identify the LSK population. LSK cells are characterized by being negative for lineage markers (Lin-) and positive for both Sca-1 and c-Kit markers. After selecting the LSK population, a Mitosox gate was applied to identify cells that have taken up the Mitosox dye. Mitosox is a fluorescent dye that accumulates in mitochondria in the presence of superoxide, providing a readout for mitochondrial oxidative stress. The Mitosox gate was set based on fluorescence intensity, comparing the staining with appropriate unstained or negative control cells.

Cre-driver	*Trp53* Status	*Mdm2* Status	Penetrance of Lymphoma	Penetrance of Leukemia
Vav-Cre	Mutant/null ¥	Wt	8/8 (100%)	0/8 (0%)
		Het	3/12 (25%) †	9/12 (75%)
	Null	Wt	7/7 (100%)	0/7 (0%)
		Het	1/7 (10%)	5/7 (71%)
	Mut/+	Wt	5/5 (100%)§	0/5 (0%)
		Het	0/4 (0%)	2/4 (50%)
Mx1-Cre	Mutant/null	Wt	5/10 (50%)‡	10/10 (100%)
		het	0/12 (0%)	11/12 (91%)
	Null	Wt	3/6 (50%) ‡	6/6(50%)
		Het	0/4 (0%)	3/4 (75%)
	Mut/+ *	Wt	-	-
		Het	-	-

¥ Mice harbored one allele of mutant (mut) and the other allele of *Trp53* floxed (null)
† Lack of recombination of *Mdm2* allele was confirmed by PCR.
‡ Animals exhibited normal thymus size, with a mixed phenotype of leukemia/lymphoma and expansion of lymphocytes in spleen.
§ Indicates a long duration of penetrance.
* No malignancy detected after 18 months of observation.

Supplementary table S1: Effects of *Cre*-driver, *Trp53* type, and *Mdm2* status on leukemia penetrance and subtype frequency, related to Figure 2 and Figure 3. The table illustrates the impact of various variables, including the choice of Cre-driver, p53 type (mutant, het vs. null), and *Mdm2* status, on the penetrance of leukemia and the frequency of each leukemia subtype observed in experimental animals.

Tagged Abs. description	Target	Label	Clone	Source	Cat #
CD4(Ms) 115In	CD4(Ms)	115In	RM4-5	BioLegend	100506
Ly-6G/C 139La	Ly-6G/Ly-6C	139La	RB6-8C5	BioLegend	108402
RFP 141Pr	RFP, DsRed	141Pr	Polyclonal	Rockland	600-401-379
CD11c(Ms) 142Nd	CD11c	142Nd	N418	DVS-Fluidigm	3142003B
CD41(Ms) 143Nd	CD41	143Nd	MWReg30	DVS-Fluidigm	3143009B
CD115(Ms) 144Nd	CD115	144Nd	AFS98	DVS-Fluidigm	3144012B
CD8a(Ms) 146Nd (MDA)	CD8a	146Nd	53-6.7	BioLegend	100702
CD19 148Nd (IMC)	CD19	148Nd	D4V4B	CST	90176BF
CD3e 152Sm (MDA)	CD3, CD3e	152Sm	145-2C11	BioLegend	100302
Galectin-3 153Eu	Galectin-3,	153Eu	M3/38	DVS-Fluidigm	3153026B
IFNa(Ms) 154Sm	IFNa	154Sm	RMMA-1	PBL	22100-1
CD34(Ms BM) 156Gd	CD34	156Gd	RAM34	BD	553731
CD14(Ms) 158Gd	CD14	158Gd	Sa14-2	BioLegend	123302
F4/80 159Tb (MDA)	F4/80	159Tb	BM8	BioLegend	123102
CD44 160Gd	CD44	160Gd	IM7	BioLegend	103002
Ter119 162Dy (MDA)	TER-119	162Dy	TER-119	Tonbo	70-5921-U100
CD36(Ms) 163Dy	CD36	163Dy	HM36	BioLegend	102602
Ly-6A/E 164Dy	Ly-6A/E, Sca-1	164Dy	D7	DVS-Fluidigm	3164005B
IFNg(Ms) 165Ho	IFNg	165Ho	XMG1.2	DVS-Fluidigm	3165003B
p53 165Ho	p53	165Ho	184721	R&D	MAB1355
CD117(Ms) 166Er	CD117, c-kit	166Er	2B8	DVS-Fluidigm	3166004B
CD150(Ms) 167Er	CD150, SLAM	167Er	TC15-12F12.2	DVS-Fluidigm	3167004B
Ki67 168Er	Ki67	168Er	B56	BD	556003
GFP 169Tm	GFP	169Tm	5F12.4	DVS-Fluidigm	3169009B
NK1.1(Ms) 170Er	NK1.1	170Er	PK136	DVS-Fluidigm	3170002B
CD11b 172Yb	CD11b	172Yb	M1/70	DVS-Fluidigm	3172012B
MDM2 173Yb	MDM2	173Yb	HDM2-323	Sigma	M7815
CD48(Ms) 174Yb	CD48	174Yb	HM48-1	BioLegend	103433
CD127(Ms) 175Lu	CD127, IL-7Ra	175Lu	A7R34	DVS-Fluidigm	3175006B
Ly-6C 89Y	Ly-6C	89Y	HK1.4	BioLegend	128002

Supplementary Table S2: Antibody panel for CyTOF analysis, related to Figure 3. A comprehensive list of antibodies used in the CyTOF analysis. Each antibody is listed along with its target antigen, metal conjugate, and catalog number. The panel encompasses a wide range of markers targeting various cellular surface proteins and intracellular signaling molecules, enabling the simultaneous assessment of multiple immune cell subsets and functional states.